# A back-projection method for imaging large-scale lateral variations of *Lg* coda *Q* with application to continental Africa

J. Xie and B. J. Mitchell
*Department of Earth and Atmospheric Sciences, St Louis University, 3507 Laclede, St Louis, MO 63103, USA*

## SUMMARY

A new method is developed which uses back-projection tomography to regionalize large-scale lateral variations of coda *Q* for *Lg* waves which have traversed long continental paths. Successful use of this method requires precise and stable single-trace measurements of *Lg* coda *Q* (Xie & Nuttli 1988). The method converges rapidly and requires minimal computer storage. It also allows quantitative estimation of resolution and error in imaging lateral variations of coda *Q*. The spatial resolution of this method is limited by the uneven spatial coverage of the data base, by our limited knowledge of *Lg* coda generation, and by the trade-off between the stability and the spatial resolution of the coda *Q* inversion. The method is applied to a large set of digital *Lg* coda data from Africa, where large-scale lateral variations of *Lg* coda *Q* are found to correlate well with major tectonic features. Most of Africa is stable, and like other stable regions, has relatively high coda *Q* values. The lowest values of coda *Q* are associated with the African rift system. Other regions of low-*Q* values include the Atlas mountains and Cape Fold Belt, regions of Mesozoic and younger deformation. The lateral variation of frequency dependence of *Lg* coda *Q* correlates, in most regions, with that of *Q* at 1 Hz. Our analysis of the spatial resolution of this method indicates that the resolving power of *Lg* coda *Q* imaging is comparable to that of velocity tomography using long-period surface waves. Using empirical approaches, we estimate that uncertainties in *Lg* coda *Q* and its power-law frequency dependence parameter are less than about 60 and about 0.2, respectively, for most of Africa.

Key words: *Lg* coda *Q*, back-projection tomography, Africa.

## 1 INTRODUCTION

Developments in seismic tomography in recent years have greatly advanced the study of lateral variations of velocity structure in continental areas. By contrast, little progress has been made in imaging lateral variations of *Q* of the Earth using tomographic algorithms (Nolet 1987). This is largely due to the lack of precision and stability in *Q* measurements, as well as the lack of a sufficiently large and well-distributed data base.

Vertical-component, high-frequency (~1 Hz) *Lg* waves can be treated as a superposition of higher-mode Rayleigh waves propagating within the continental crust (Knopoff, Schwab & Kausel 1973; Der *et al.* 1984; Kennett 1984). It is reasonable to assume that in the absence of large-scale disruption of the crustal wave guide, *Q* derived from *Lg* or its coda is representative of *Q* of the continental crust (e.g.

Singh & Herrmann 1983; Der *et al.* 1984; Campillo 1987). In this paper we define *Lg Q* as *Q* derived from the direct *Lg* phase and *Lg* coda *Q* as *Q* derived from *Lg* coda. Measuring *Lg Q* requires either records from two stations on the same great circle path or a record from one station produced by an event for which we have knowledge of the source spectrum (Cheng & Mitchell 1981; Campillo 1987). With data currently available, these requirements will likely result in very poor ray path coverage for studying lateral variations of *Q*. *Lg* coda *Q* can, however, be measured at a single station without knowledge of the source spectrum (Aki & Chouet 1975; Herrmann 1980; Xie & Nuttli 1988); it is therefore more useful than *Lg* itself for the study of large-scale lateral variations of *Q*. The interpretation of *Lg* coda, however, is more difficult than that of *Lg*. Because high-frequency coda is highly random, it is difficult to model *Lg* coda properly and regionalized coda *Q* values resulting
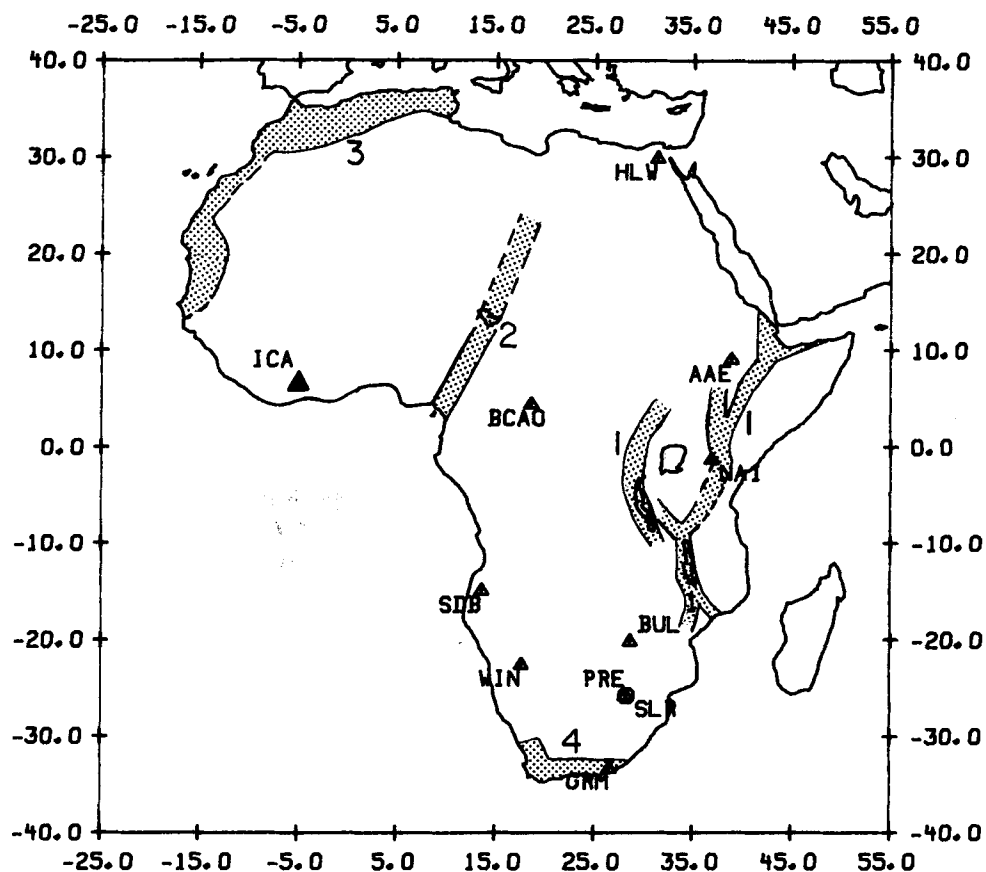
161

**Figure 1.** Map showing the locations of seismographic stations used in this study (triangles and circles), and areas that have been affected by orogenies or large-scale rifting in the last 425 million years (shaded areas): 1, the East African Rift system; 2, the Cameroon rift (or the Cameroon volcanic line) system; 3, the Atlas Mountains; 4, the Cape Fold Belt. Adopted from Clifford (1970), Dott & Batton (1971) and Cahen *et al.* (1984). ICA indicates the Ivory Coast Array.

from inversion may be characterized by large uncertainties. Nevertheless, several studies have determined lateral variations of *Lg* coda *Q* (or local coda *Q* derived from local *S*-wave coda) in major continental areas such as North and South America and China, using a master curve technique (Herrmann 1980; Singh & Herrmann 1983; Raoof & Nuttli 1985; Jin & Aki 1988). The results of these studies generally show good correlation between lateral variations of *Q* and the main tectonic features of the continents studied.

In order to improve the precision and stability of *Lg* and *Q* measurements, Xie & Nuttli (1988) proposed a stochastic model for *Lg* coda. They discussed the effects of various physical processes (e.g. dispersion, mode conversions, scattering) which affect the generation of *Lg* coda. They approximated the randomness of *Lg* coda by band-limited white, Gaussian noise. This approach allows a quantitative estimate of the variance of *Q* determined by the inversion process. A stacked spectral ratio (henceforth denoted as SSR) method was proposed for *Lg* coda *Q* inversion which allows cancellation of station site effects (provided that those effects are stationary) and results in a large reduction of the variance. Improved *Q* values obtained by the SSR method, plus the rapid evolution of techniques used in seismic tomography, make it possible to develop more quantitative, or computerized, methods to image lateral variations of *Lg* coda *Q*, with more rigorous analysis of error and resolution.

Africa is a continent where no systematic investigation of crustal *Q* has been conducted. Almost all of Africa has been free of orogenic activity for about the past 500 million years (Clifford 1970; Cahen *et al.* 1984). Africa has some unique and interesting tectonic features, the most striking being the well-developed rift systems and volcanic lines (Moreau *et al.* 1987) in east and west Africa, with lengths of thousands of kilometres (Fig. 1). Other noteworthy features of this continent are the younger mountain ranges at both the southern and northern margins. The Cape Fold Belt in the south and the Atlas mountains in the north were affected by Hercynian or younger orogenies.

## 2  INVERSE METHODS

As in velocity tomography, the imaging of lateral variations of *Lg* coda *Q* proceeds in two steps. First, individual seismograms containing coda are collected and processed to obtain *Q* values, each being a functional of the distribution of regional *Lg Q* (or more strictly, of regional *Lg* coda *Q*) inside an area sampled by the single-trace coda record. Second, many single-trace measurements are combined to image the lateral variations of *Q*. A major difference between *Lg* coda *Q* tomography and velocity tomography is that the forward modelling involved in the former method must take into account the elliptical region over which

scattering occurs whereas the latter considers seismic waves that are restricted to single paths.

## 2.1 Single-trace measurement of coda $Q$

High-frequency coda is highly random and the generation of $Lg$ coda involves various complicated physical processes such as scattering, dispersion, mode summation and mode conversion (Der *et al.* 1984; Snieder 1987; Xie & Nuttli 1988). Consequently, two problems arise in the interpretation of the single-trace coda records. First, because of the randomness of coda it is difficult to obtain a $Q$ estimator which is stable enough to provide an acceptable variance (Der *et al.* 1984). Second, a coda $Q$ estimator may be subject to systematic deviations from an $Lg\,Q$ estimator due to imprecise forward modelling. In order to solve these two problems Xie & Nuttli (1988) derived a stochastic model and an inverse method for the interpretation of single-trace $Lg$ coda signals. They used a convolutional relationship to model the processes of $Lg$ coda generation. That relationship allows the effect of those processes to be expressed and examined separately in the frequency domain. In particular, they found that the single isotropic scattering (SIS) model can satisfactorily explain previous observations on several major continents, and that the randomness of the $Lg$ coda signal can be approximated by simple band-limited white, Gaussian noise. The latter approximation allows a quantitative estimation of the theoretical variance of coda $Q$ inversion. Xie & Nuttli (1988) found that unacceptably low confidence levels in the $Lg$ coda $Q$ inversion results could occur if a carefully designed variance reduction procedure was not used. At large epicentral distances the problem of low confidence levels can be very serious due to the narrow pass-band of the $Q$ filter. They therefore proposed a SSR method to reduce the variance resulting from the inversion. For convenience of discussion we briefly summarize the SSR method in the following paragraphs.

First, the $Lg$ coda time series is divided by a number, $N_{\mathrm{W}}$, of non-overlapping time windows with a constant window length, $T$, where the $m$th window has a centred lapse time $\tau_m$, and $m = 1, 2, \ldots, N_{\mathrm{W}}$. For each window of the time series the discrete Fourier transform is performed to obtain the geometrical mean of the amplitude spectrum, $\langle A_{k,m} \rangle$, at the $k$th discrete frequency $f_k = k/T$, defined as

$$\langle A_{k,m} \rangle = \prod_{i=k-l}^{k+l} |A_{i,m}|^{1/(2l+1)}, \tag{1}$$

where the subscripts $i$ and $k$ represent discrete frequencies, and $m$ denotes the window number. $|A_{i,m}|$ is the $i$th discrete amplitude spectral estimate obtained by applying the discrete Fourier transform to the $m$th windowed time series and $2l + 1$ is an integer, which gives the number of amplitude spectral estimates used in each geometrical mean.

The SSR is defined as

$$F_k = \frac{1}{M} \sum_{m=1}^{M} \frac{1}{\pi(\tau_{M+m} - \tau_m)} \log\left[\frac{G_{M+m}\sqrt{U_m}\langle A_{k,m}\rangle}{G_m\sqrt{U_{M+m}}\langle A_{k,m+M}\rangle}\right], \tag{2}$$

where $M$ is given by

$$M = \begin{cases} N_{\mathrm{W}}/2 & \text{if } N_{\mathrm{W}} \text{ is even} \\ (N_{\mathrm{W}}+1)/2 & \text{if } N_{\mathrm{W}} \text{ is odd} \end{cases} \tag{3}$$

$U_m$ is the length of each group velocity window for $Lg$ given by

$$U_m = v\tau_m(1/v_{\min} - 1/v_{\max}) \tag{4}$$

where $v$, $v_{\max}$ and $v_{\min}$ are the average, maximum and minimum group velocities of the $Lg$ wave train, respectively: $G_m$ is the geometrical spreading term which can be expressed as

$$G_m = \left[\frac{1}{4\pi^2 R\sqrt{v^2 t^2/R^2 - 1}}\bigg|_{t=\tau_m} \Delta\phi\right]^{-1/2}, \tag{5}$$

where $\Delta\phi$ is given by

$$\Delta\phi = \int_{\phi=\phi_1}^{\phi_2} d\phi = \phi_2 - \phi_1. \tag{6}$$

We have replaced the symbol $\eta$ in Xie & Nuttli (1988) by $\phi$ in order to avoid confusion with the frequency dependence of $Q$ in equation (7) of this paper. Equation (6) is obtained using equations (A1) through (A5) of Xie & Nuttli (1988) but is more general than equation (A5) because here we have generalized the limits of integration for $\phi$. When part of the integration path, which is an ellipse, is missing, the numbers $\phi_1$ and $\phi_2$ can be found using equation (A4) of Xie & Nuttli (1988). An example of this situation is the case when the ellipse intercepts a continental boundary which is non-transmissive to $Lg$ waves. Otherwise $\Delta\phi$ is $2\pi$ and the resulting $G_m$ from equation (5) becomes

$$G_m = (2\pi R)^{-1/2}(v^2\tau_m^2/R^2 - 1)^{-1/4}. \tag{5'}$$

The right-hand side of equation (2) is calculable from a coda time series.

Assuming a power law for the frequency dependence of $Q$

$$Q(f) = Q_0 f^\eta, \tag{7}$$

where $Q_0$ and $\eta$ are $Q$ at $1\,\mathrm{Hz}$ and the frequency dependence of $Q$, respectively, Xie & Nuttli (1988) used linear regression to find $\eta$ and $Q_0$ from

$$\log F_k = (1 - \eta)\log f_k - \log Q_0 + \epsilon, \tag{8}$$

where $\epsilon$ represents a random error. Both theoretical and observational calculations show that the SSR provides a statistically stable $Q$ estimator, with the resulting standard error in $Q_0$ being an order of magnitude smaller than $Q_0$ itself.

A possible source of major systematic deviations of the $Lg$ coda $Q$ estimator from the $LgQ$ estimator is the use of an incorrect geometrical spreading term, $G_m$ in equation (2). Using available observations conducted in various areas, including central Asia, North America and southern Africa, Xie & Nuttli (1988) made a comparison between the $LgQ_0$ and $Lg$ coda $Q_0$ calculated from applying the SIS model to digital coda data, and concluded that the geometrical spreading term $G_m$ calculated using the SIS model can be used to calculate the value of $Lg$ coda $Q_0$ and that that value is close to $LgQ_0$ averaged over the same area. These areas have widths of about $10^3\,\mathrm{km}$. This conclusion is semi-empirical and many aspects on the generation of $Lg$ coda still remain unclear. For instance, we do not yet understand the details of mode conversion, nor why the SIS model appears to be valid. A further

complication is that the stochastic modeling of *Lg* coda may be non-unique (Xie & Nuttli 1988).

## 2.2  Spatial interpretation of single trace coda *Q* measurements

In order to obtain an image of lateral variation of *Lg* coda *Q* which closely resembles the lateral variation of *LgQ*, one has to interpret single-trace measurements of *Lg* coda *Q* in terms of laterally varying *LgQ*, i.e. one has to make an *a priori* assumption about how the single-trace measurements of *Lg* coda *Q* depend on the laterally varying *LgQ* inside the area sampled by *Lg* coda. From considerations of the afore-mentioned non-uniqueness in modelling *Lg* coda and the unclear aspects of *Lg* coda generation, we think it is premature to assume a detailed, perhaps non-linear, functional relationship of such a dependence to image lateral variation of *LgQ*. Additional problems in any attempt at using such a detailed functional relationship comes from the tremendous computation time and computer storage involved, and the probability of numerical instabilities (Xie & Mitchell 1988). On the other hand, the *Lg* coda time series is typically longer than 300 s, thus the moving window stacking defined by equation (2) utilizes many windows and results in a stable measurement of *Q*. Assuming an *Lg* group velocity of 3.5 km s$^{-1}$ and single scattering, the area sampled by the single trace *Lg* coda will always have a width greater than $10^3$ km. This distance is about the same as the widths of the areas over which the consistency between averaged $LgQ_0$ and *Lg* coda $Q_0$ were observed (Section 2.1). Therefore we assume that the inverse of *Lg* coda *Q* obtained by applying the SSR method (with $G_m$ calculated from the SIS model) to a single-trace record of *Lg* coda gives the areal average of $LgQ^{-1}$ inside the elliptical area corresponding to the maximum $\tau_m$, which will be denoted as $\tau_{max}$, of this record. The major and minor axes of this ellipse are given respectively by

$$a = ct/2|_{t=\tau_{max}}, \tag{9}$$

where $v$ is the same as in equation (4), and

$$b = \sqrt{v^2t^2 - R^2}|_{t=\tau_{max}}, \tag{10}$$

where $R$ is the epicentral distance [Xie & Nuttli 1988, equations (A3) and (A4); note that $r_1 + r_2 = vt$ and that the delta function in equation (A3) results in $\alpha$ being equal to $vt/R$].

Since the $\tau_{max}$ of a coda record, under the single-scattering assumption, gives the largest possible area sampled by the *Lg* coda, the above assumption attributes each coda *Q* value measured from a single-trace record to the average *LgQ* over the largest possible area. We will use this assumption exclusively in imaging lateral variations of *Q*. Strictly speaking the image of lateral variations of *Q* obtained using such an assumption is the image of lateral variations of *Lg* coda *Q*, which, as indicated in the above discussion, should closely resemble the lateral variations of *LgQ*.

It appears that the above assumption will lead to limited resolving power in the imaging of lateral variation of coda *Q*. Previous practice in determining lateral variations of coda *Q* (Singh & Herrmann 1983; Raoof & Nuttli 1985; Jin

& Aki 1988) have assigned single-trace *Q* measurements to spatial points, instead of areas. We think that our assumption is more reasonable since high-frequency seismic coda samples an area rather than a spatial point. Moreover, spatial resolution in imaging lateral variations of coda *Q* is also limited by the random nature of the high-frequency coda signal. This causes more basic and more severe restrictions in resolution compared to any restrictions artificially caused by the assumptions used in our inversion. This basic restriction is very important and profound but has not been addressed previously. We shall give a detailed discussion on this limitation in the following paragraphs.

There is a trade-off between the stability of single-trace coda *Q* measurements and spatial resolution. As mentioned by Kopnichev (1980), Der *et al.* (1984) and Xie & Nuttli (1988), the high-frequency *Lg* coda is highly random. Thus in order to estimate coda *Q* using spectral ratios, stacking techniques should be used to overcome large variances or uncertainties. Stacking can be applied either to coda data from repeated paths if they are available, or to coda obtained from many time-shifted windows applied to the same single trace. Moving-window stacking (Xie & Nuttli 1988) can provide better data coverage since only one record is required for multiple measurements. In this method, as one moves toward later parts of the coda, the area sampled by the signal successively increases and the spatial resolution becomes poorer. This is a special case of the usual trade-off between variance and resolution in inverse problems (Backus & Gilbert 1970). In measuring coda *Q* using the master curve method (Herrmann 1980), better constrained coda *Q* estimates require use of predominant frequencies measured from the later part of coda, unless *Q* is very low (Singh & Herrmann 1983; Xie & Nuttli 1988). The method of Aki & Chouet (1975) applies linear regression to amplitudes over lapse time for each of several frequency pass-bands. More data points are needed in these regressions to reduce the uncertainty in the estimation of slope (which gives *Q*); thus the later part of coda is also needed in the method of Aki & Chouet (1975). Therefore to stabilize the *Q*-inversion using the random coda signal, the later part of coda is needed, regardless of the method used. The increased stability and the reduced uncertainty due to using the later coda, however, is achieved at the cost of poorer spatial resolving power of later coda since it samples a larger area. Eventually one achieves an acceptable uncertainty in coda *Q* inversion with limited spatial resolution. Compared to this primary limitation in the spatial resolution inherent in narrow-band random coda signal, the limitations associated with our assumptions are secondary and probably trivial. At short distances the low-pass effect of attenuation is not as serious as it is at large distances where *Lg* coda is observed; therefore for local *S*-wave coda recorded by broad-band instruments, the variance could be reduced by increasing $2l + 1$ (equation 1) at the cost of frequency resolution if the SSR method is used, and the trade-off could be set toward a higher spatial resolution.

## 2.3  Method of imaging lateral variations of *Lg* coda *Q*

In this section we propose a back-projection algorithm to image lateral variations of *Lg* coda *Q*. Suppose we have a

number ($N_d$) of $Lg$ coda time series collected from a continental region. We shall denote the $Q$ value calculated by applying the SSR method to the $n$th time series by $\overline{Q_n}$. We divide the whole area under study into a number of $N_g$ grids with widths of $W_{NS}$ degrees in a north–south direction and $W_{EW}$ degrees in an east–west direction. We parametrize the unknown lateral variation of $Lg$ coda $Q$ by assuming it to be a constant ($Q_m$) inside the $m$th grid. Following the assumption in Section 2.2, $\overline{Q_n}$ gives the areal average of $LgQ$ (strictly speaking, $Lg$ coda $Q$) in the elliptical area sampled by coda waves received at the maximum lapse time, $\tau_{max}$, of the whole time trace. Denoting the area that the $n$th ellipse overlaps with the $m$th grid by $s_{mn}$, we have

$$\frac{1}{\overline{Q_n}} = \frac{1}{S_n} \sum_{m=1}^{N_g} \frac{s_{mn}}{Q_m} + \epsilon_n, \qquad n = 1, 2, \ldots, N_d, \tag{11}$$

where

$$S_n = \sum_{j=1}^{N_g} s_{jn}$$

and $\epsilon_n$ is the residual due to the errors in modelling $Lg$ coda and in the $Q$ measurement. Equation (11) is a sparse linear system because many of the $s_{mn}$'s are zero. We shall use a back-projection, or ART technique (e.g. Gordon 1974; Dines & Lytle 1979; McMechan 1984; Suetsugu & Nakanishi 1985; Humphreys & Clayton 1988) to solve equation (11). This technique is an iterative 'raw-action' procedure. Our adopted version of this technique to image lateral variation of $Lg$ coda $Q$ is briefly summarized as follows.

(i) Calculate $s_{mn}$ for all the $(m, n)$'s and store all the non-zero $s_{mn}$ values.

(ii) Construct a starting model for $Q_m$'s, denoted by $Q_m^i$, for $m = 1, 2, 3, \ldots, N_g$, and $i = 0$ (the superscript $i$ will be used to indicate the last iteration completed over all the coda records).

(iii) For each of the $n$ records ($n = 1, 2, 3, \ldots, N_d$), calculate the updated residual $\Delta_n^i$, defined through

$$\Delta_n^i = \frac{S_n}{\overline{Q_n}} - \sum_{m=1}^{N_g} \frac{1}{Q_m^i} s_{mn}. \tag{12}$$

(iv) For each of the $m$ grids ($m = 1, 2, \ldots, N_g$), a new estimate of $Q_m$, denoted by $Q_m^{i+1}$, is made by back projecting $\Delta_n^i$ into the inverse of the $Q_m^i$'s:

$$\frac{1}{Q_m^{i+1}} = \frac{1}{Q_m^i} + \frac{1}{N_i} \sum_{n=1}^{N_d} \frac{\Delta_n^i s_{mn}}{\sum_{j=1}^{N_g} s_{jn}^2}. \tag{13}$$

(v) A nine-point spatial smoothing proposed by Suetsugu & Nakanishi (1985) is applied to smooth and stablize the inversion. If we denote the $m$th grid by $m(l, j)$, where $l$ and $j$ are grid numbers in the east and north directions,

respectively, then the smoothed model $(Q_{m(l,j)}^{i+1})'$ is given by

$$\frac{1}{(Q_{m(l,j)}^{i+1})'}$$

$$= \frac{1}{29}\left[\frac{1}{Q_{m(l-1,j-1)}^{i+1}} + \frac{1}{Q_{m(l-1,j+1)}^{i+1}} + \frac{1}{Q_{m(l+1,j-1)}^{i+1}} \right.$$

$$+ \frac{1}{Q_{m(l+1,j+1)}^{i+1}} + 4\left(\frac{1}{Q_{m(l,j-1)}^{i+1}} + \frac{1}{Q_{m(l,j+1)}^{i+1}}\right)$$

$$\left. + \frac{1}{Q_{m(l-1,j)}^{i+1}} + \frac{1}{Q_{m(l+1,j)}^{i+1}}\right) + \frac{9}{Q_{m(l,j)}^{i+1}}\right]. \tag{14}$$

This smoothing procedure is much like a spatial Gaussian filter, and we have found that unreasonably low (or even negative) $Q^{-1}$ values could result if this smoothing is not applied.

(vi) Repeat the iterative procedures in (iii)–(v) until one of the following criteria is satisfied:

$$i + 1 \geq i_{max}, \tag{15}$$

or

$$\frac{\sum_{j=1}^{N_d} (\Delta_j^{i+1})^2 - \sum_{j=1}^{N_d} (\Delta_j^i)^2}{\sum_{j=1}^{N_d} (\Delta_j^i)^2} \leq \delta^2 \tag{16}$$

where $i_{max}$ is an integer which gives the maximum iteration acceptable and $\delta$ is the relative change in the overall residual, or the relative improvement of the degree to which the model fits data. Both numbers were chosen by experience after several tests of the method. Both $i_{max}$ and $\delta$ are set before the iteration procedure begins.

The advantages of using back-projection techniques include the minimal computer storage involved, and the rapid convergence achieved. These advantages are very important when an entire continent is being studied. The disadvantage of using this technique is that back-projection does not provide formal estimates of resolution, bias and error (Suetsugu & Nakanishi 1985). Humphreys & Clayton (1988) suggested using the 'point spreading function', which we shall denote as p.s.f., as an approximation of the resolution kernel. To obtain the p.s.f. one simply constructs a model composed of one grid with unit-valued $Q^{-1}$ at the geographic point of interest. The $Q^{-1}$ values in all the other grids are set at zero. Synthetic data using this model are then computed and inverted. The resulting image gives the p.s.f. at this geographic point, which in turn gives a measure of spreading of the resolution kernel.

The effect of random noise preserved in single-trace $Q$ estimates on the final image can be empirically tested utilizing the sample standard error in $\overline{Q_n}$ due to the randomness of SSRs (Xie & Nuttli 1988). To do so we denote the standard error associated with $\overline{Q_n}$ by $\delta Q_n$, $n = 1, 2, 3, \ldots, N_d$ (note that $\delta Q_n$ is always positive due to the way standard error is estimated), and assume that $\delta Q_n$ gives a good measure of the absolute value of real error preserved in the corresponding $\overline{Q_n}$ measurements. We then empirically construct a number, $N_d$, of noise series, whose $n$th member have an absolute value equal to $\delta Q_n$ and a sign that is chosen randomly. The $n$th term of this noise series is

then added to $\overline{Q_n}$, which we shall denote as

$$\overline{Q_n'} = \overline{Q_n} + \delta Q_n.$$

$\overline{Q_n'}$ values were then inverted to obtain a new $Q_m$ model. The difference between the new image of $Q_m$ values using $\overline{Q_n'}$ and the original image of $Q_m$ values will give us an error estimation for the $Q_m$ values. This process empirically measures the effect of random noise on the $Q_m$ image. The sign of the $\delta Q_n$ series can be simulated by psuedorandom binary generators in a computer and the process must be repeated several times to obtain an averaged, and more stable error measurement of $Q_m$ values.

## 3   DATA PROCESSING

In this study we have used $Lg$ coda records collected from vertical-component, short-period seismographs installed at 12 stations in continental Africa. Table 1 lists the instrument types of these seismographs, and the codes and locations of the stations. The station locations are also plotted in Fig. 1, where the Ivory Coast Array stations are clustered together and abbreviated as ICA. The data set is composed of the following.

(i) 59 digital records from stations BCAO and SLR, both belonging to the DGSN network. Events recorded by these stations occurred in the years 1979 through 1985.

(ii) 155 analogue records from WWSSN stations AAE, BUL, GRM, HLW, NAI, PRE, SDB and WIN. Events recorded by these stations occurred primarily in the years 1973 and 1974, but two nuclear explosions occurred on 1963, October 20 and 1965, February 27.

(iii) 39 analogue records from the Ivory Coast Array stations. Twelve events recorded at these stations occurred during the years 1978 through 1984. The Ivory Coast Array has five short-period ($\sim 1$ Hz), vertical seismographs with an instrument response similar to that of WWSSN instruments. These seismographs are located within tens of kilometres of each other. Four of them are high-gain instruments (magnification $\geq 125$ k), and one is low-gain (magnification $= 62.5$ k). We have chosen to use three or four (depending on how many were available to us with acceptable record length and signal/noise ratios) of the records from the high-gain instruments in this study. The response of these instruments varied quite frequently during the years of recording events, but these variations have no effect when the SSR method is used (Xie & Nuttli 1988).

**Table 1.** Seismographic stations used in this study.

| Station Code | Latitude | Longitude | Type of Instrument† |
|---|---|---|---|
| AAE | 9.0300 ° N | 38.8000 ° E | WWSSN |
| BCAO | 4.4335 ° N | 18.5354 ° E | SRO |
| BUL | 20.1430 ° S | 28.6130 ° E | WWSSN |
| DIC | 6.6700 ° N | 4.7700 ° W | IC * |
| GRM | 33.3133 ° S | 26.5733 ° E | WWSSN |
| HLW | 29.8580 ° N | 31.2420 ° E | WWSSN |
| KIC | 6.3606 ° N | 4.7411 ° W | IC * |
| LIC | 6.2244 ° N | 5.2778 ° W | IC * |
| NAI | 1.2739 ° S | 36.8037 ° E | WWSSN |
| PRE | 25.7533 ° S | 28.1900 ° E | WWSSN |
| SLR | 25.7349 ° S | 28.2816 ° E | DWWSSN |
| TIC | 6.6447 ° N | 5.0200 ° W | IC * |
| WIN | 20.1430 ° S | 28.6130 ° E | WWSSN |

† all instruments are short period, vertical component

* Ivory Coast Stations. These instruments have responses similar to that of 1-Hz short-period WWSSN instruments.

All of the analogue seismograms were digitized at St Louis University. Figs 2 and 4 display some typical digitized seismograms from WWSSN and Ivory Coast Array stations, respectively. Together with the digital seismograms, we have a total number of 253 $Lg$ coda time series. This makes the digital $Lg$ coda data set used in this study the largest ever collected for a major continent. Each of the coda time series were segmented by many windows with the centred lapse time, $\tau_m$, starting at roughly the arrival of group velocity of $3.15$ km s$^{-1}$ and increasing to successively cover the entire portion of the signal which can be distinguished from the ambient noise. We used a 10 per cent Hanning window with a length of 30 s for the digitized analogue data and a length of 25.6 s for the digital GDSN data. The reference noise spectra for each record were obtained in the way described by Xie & Nuttli (1988), i.e., from the portion of the trace prior to the $P$ arrival. The Fast Fourier transform (FFT) was performed on both signal and noise and the effect of noise was empirically reduced by subtracting the reference power spectra of noise from power spectra of the signal. The SSR, defined by equation (2), was then obtained for single-trace $Q$ measurements. Table 2 lists the event dates, recording stations, epicentral distances, back-azimuths and the resulting single-trace measurements of $Lg$ coda $Q$, together with the estimated standard errors. Fig. 3 gives some examples of the SSR analysis using the digitized WWSSN records displayed in Fig. 2. The frequency band used is from 0.5 to 2.0 Hz. It is noteworthy that the SSR estimated from the event dated 1974 May 5 recorded by station BUL (middle of Fig. 1) fluctuated more than others, perhaps because of fundamental-mode interference. Some examples of SSR analysis using GDSN data can be found in Xie & Nuttli (1988). All of the events recorded by the Ivory Coast Array were a few thousand kilometres from the stations, giving virtually the same traveltimes to all the stations (Table 1). In this case we have treated the records of the same event collected from all the available stations belonging to this array as records of a repeated path and obtained a more stable $Q$ measurement by averaging the SSR over the whole array. This permitted us to use a shorter coda time series (roughly 200–300 s), but to still have rather small sample standard errors. Figs 4 and 5 give examples of this averaging process. Fig 4 shows the time traces and Fig. 5 shows the SSRs calculated from each station (curves), their average (dots) and the linear regression over the average (line), together with the resulting $Q_0$ and $\eta$ (denoted by $z$ in the plot), and their standard errors.

The lengths of the coda time series we used are between 200 and 800 s. We have determined the sampling areas of these coda records under the assumptions that each coda time series samples an elliptical area with axes given by equations (9) and (10) and that the boundary separating oceanic crust from continental crust forms a non-transmissive barrier to the $Lg$ wave. When such a boundary is encountered by the $Lg$ wave coming from the continental side, some part of the energy carried by this wave is scattered back into the continental side and the remaining energy is converted into other types of seismic waves which propagate into the oceanic crust or mantle. We further assume that the scattering at this boundary is isotropic and is not abnormally strong, compared to the scattering caused by
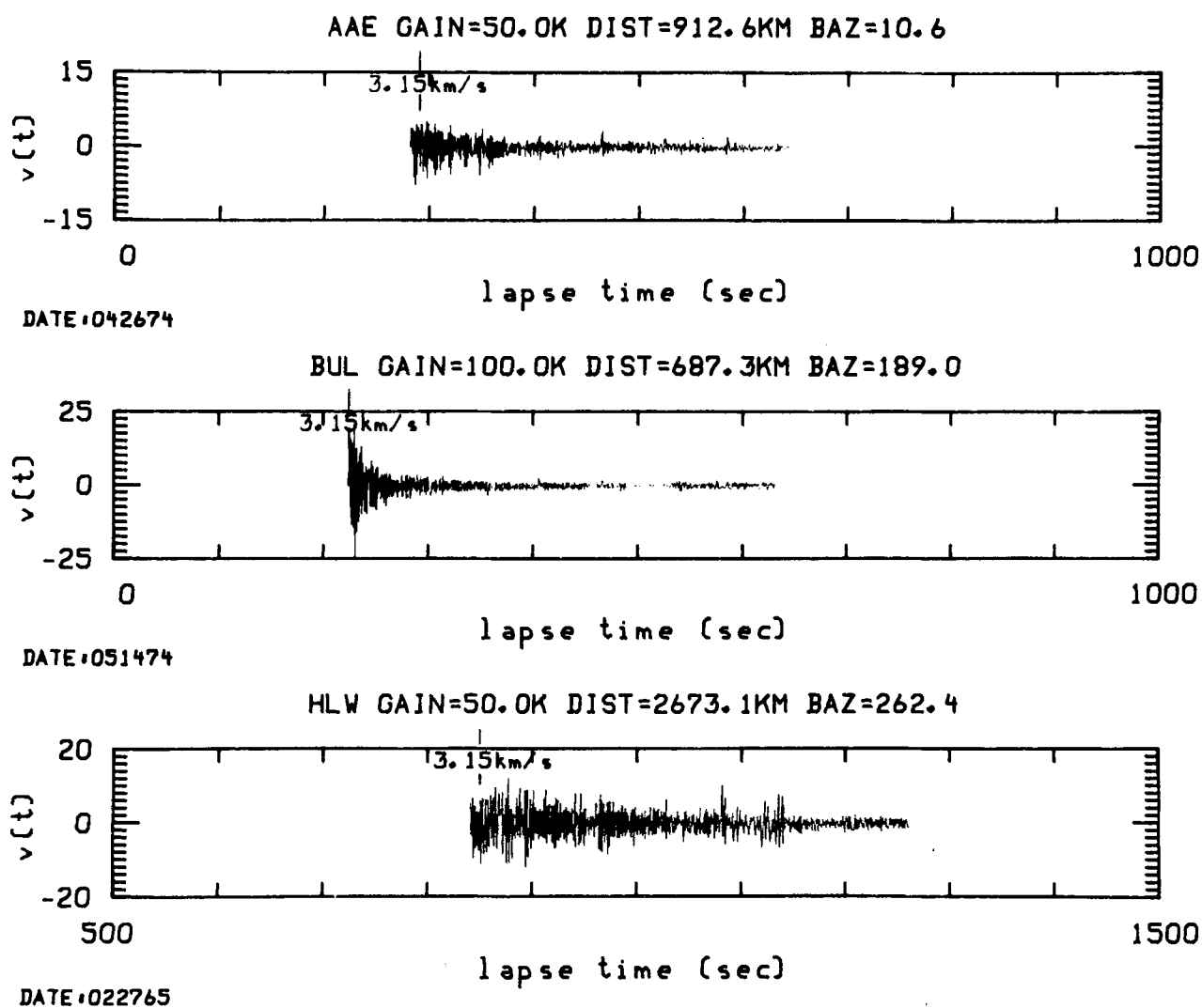
AAE GAIN=50.0K DIST=912.6KM BAZ=10.6

DATE:042674

BUL GAIN=100.0K DIST=687.3KM BAZ=189.0

DATE:051474

HLW GAIN=50.0K DIST=2673.1KM BAZ=262.4

DATE:022765

**Figure 2.** Three typical short-period, vertical-component WWSSN seismograms showing $Lg$ coda. The abscissa indicates the lapse time measured from the earthquake origin time. The seismograms were digitized from analogue records. The station code, gain of the instrument, epicentral distance and back-azimuth (in degrees) are shown above each trace. The event date is indicated below each trace and the arrival times of group velocities of $3.15\,\mathrm{km\,s^{-1}}$ are identified.

$Q_0 = 533 +/- 49 , z = 0.4 +/- 0.1$

$Q_0 = 687 +/- 81 , z = 0.4 +/- 0.1$

$Q_0 = 842 +/- 63 , z = 0.2 +/- 0.1$

AAE.042674

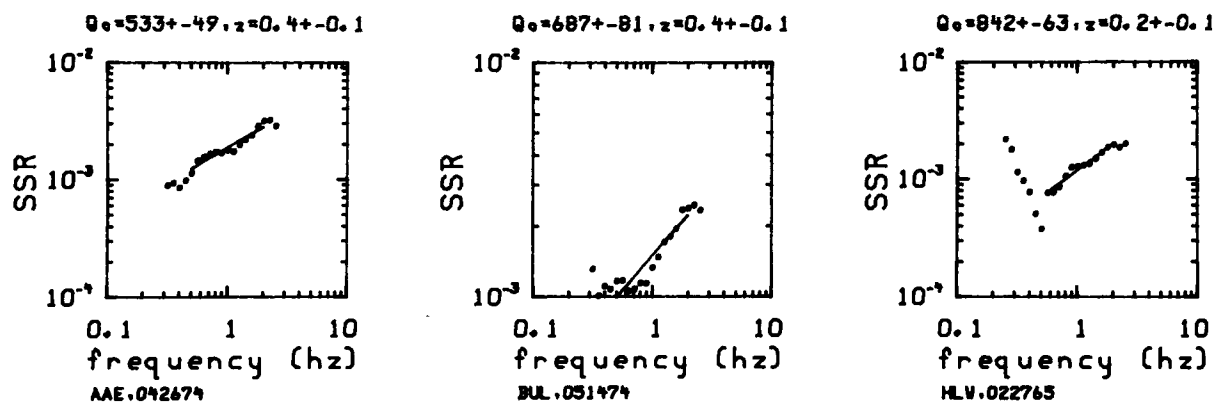BUL.051474

HLW.022765

**Figure 3.** $Q_0$ and frequency dependence (denoted by $\eta$ in text and by $z$ in this plot) values and their standard errors obtained by linear regression using SSR values calculated from the records plotted in Fig. 2. The frequency band used is 0.5–2.0 Hz. At lower frequencies the spectral ratio estimates in the middle plot (station BUL) shows some fluctuations, probably due to the fundamental-mode interference.
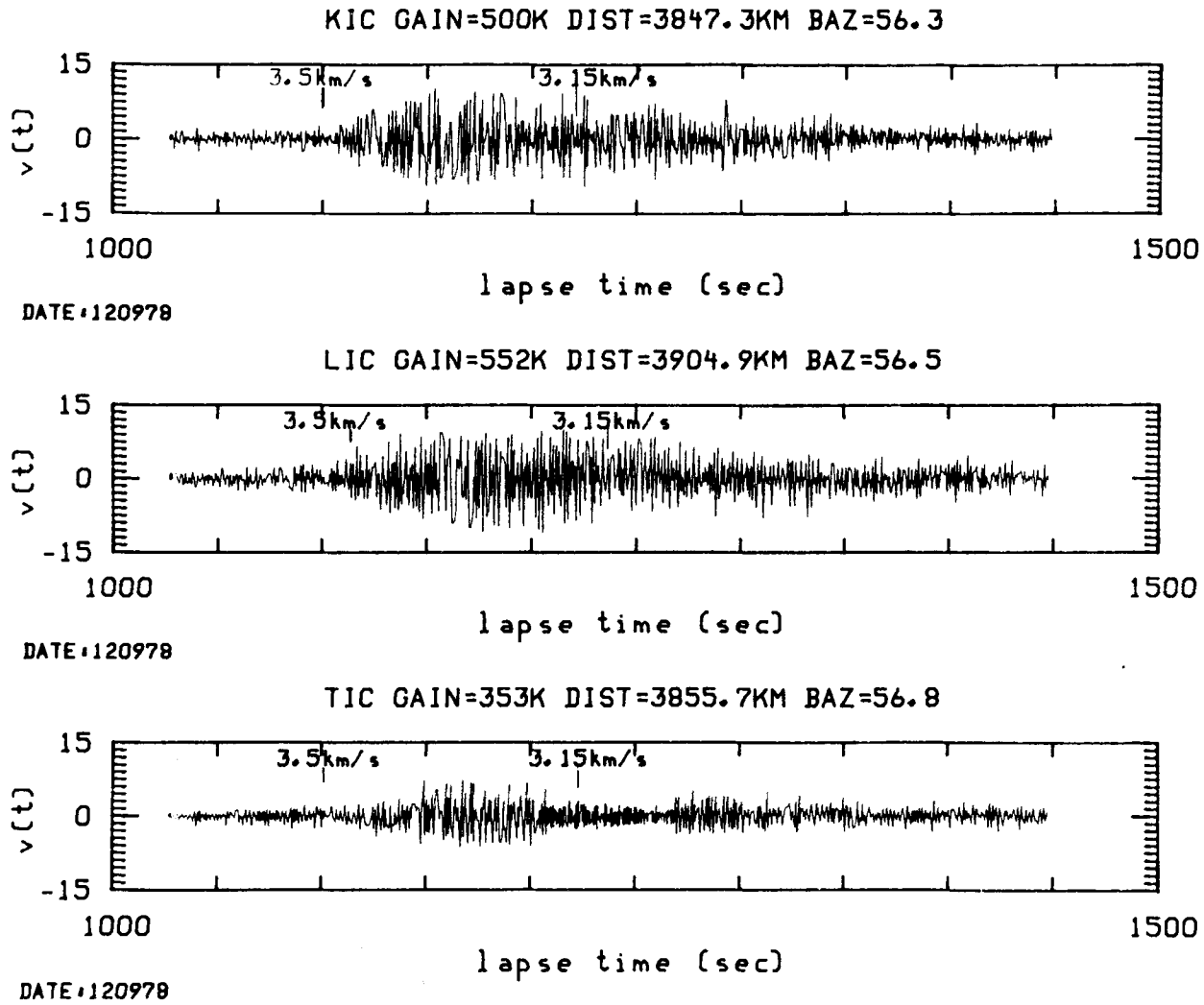
KIC GAIN=500K DIST=3847.3KM BAZ=56.3



DATE·120978

LIC GAIN=552K DIST=3904.9KM BAZ=56.5



DATE·120978

TIC GAIN=353K DIST=3855.7KM BAZ=56.8



DATE·120978

**Figure 4.** Typical short-period, vertical-component seismograms at three Ivory Coast Array stations showing the long duration of $Lg$ and $Lg$ coda. The abscissa indicates the lapse time. The event is the same for all of the traces. The station code, instrument gain, epicentral distance, and back-azimuth (in degrees) are above each trace. The event date is indicated below and near the beginning of each trace, and the arrival times of waves with group velocities of 3.50 and 3.15 km s$^{-1}$ are identified.

**Table 2.** Events used and the corresponding results of single-trace analysis of $Lg$ coda $Q$, with sample standard errors.

| Event Date | Origin Time + | Recording Station | Epicentral Distance(km) | Back Azimuth | $Q_0$ | $\eta$ |
|---|---|---|---|---|---|---|
| 102063 | 13h0m0.0s | AAE | 3948.9 | 299.0 | 724 ± 67 | 0.3 ± 0.2 |
| 022765 | 11h30m0.0s | AAE | 3949.5 | 299.0 | 690 ± 91 | 0.4 ± 0.2 |
| 010773 | 12h17m12.6s | AAE | 468.2 | 207.5 | 454 ± 40 | 0.5 ± 0.1 |
| 011373 | 6h5m42.2s | AAE | 3076.5 | 201.9 | 510 ± 83 | 0.5 ± 0.1 |
| 011473 | 13h36m59.8s | AAE | 1991.2 | 208.5 | 461 ± 53 | 0.5 ± 0.1 |
| 030573 | 23h59m46.6s | AAE | 2133.2 | 346.0 | 712 ± 89 | 0.3 ± 0.2 |
| 040173 | 6m29m27.7s | AAE | 534.2 | 57.4 | 449 ± 49 | 0.5 ± 0.1 |
| 040573 | 1h59m12.6s | AAE | 906.0 | 66.2 | 493 ± 54 | 0.5 ± 0.1 |
| 040773 | 19h17m38.7s | AAE | 530.0 | 55.0 | 518 ± 34 | 0.5 ± 0.1 |
| 041373 | 14h13m56.9s | AAE | 633.4 | 59.0 | 468 ± 61 | 0.5 ± 0.1 |
| 041573 | 13h13m33.4s | AAE | 2024.7 | 208.1 | 452 ± 61 | 0.5 ± 0.3 |
| 042273 | 22h3m43.5s | AAE | 1014.1 | 236.6 | 499 ± 52 | 0.5 ± 0.1 |
| 051473 | 20h16m26.8s | AAE | 1951.7 | 210.7 | 475 ± 56 | 0.5 ± 0.1 |
| 052473 | 7h15m8.5s | AAE | 2211.0 | 194.7 | 478 ± 75 | 0.5 ± 0.2 |
| 070773 | 16h4m9.9s | AAE | 1387.7 | 195.2 | 425 ± 62 | 0.6 ± 0.2 |
| 071873 | 19h39m13.0s | AAE | 2285.0 | 192.2 | 477 ± 55 | 0.5 ± 0.2 |
| 112473 | 14h5m46.4s | AAE | 4591.5 | 316.1 | 810 ± 109 | 0.3 ± 0.2 |
| 120173 | 16h51m14.0s | AAE | 1383.3 | 228.5 | 441 ± 59 | 0.5 ± 0.2 |
| 021874 | 9h59m45.7s | AAE | 1704.1 | 217.7 | 453 ± 65 | 0.5 ± 0.1 |
| 031774 | 7h31m25.2s | AAE | 995.0 | 298.9 | 683 ± 53 | 0.4 ± 0.1 |
| 041774 | 18h27m33.7s | AAE | 924.7 | 10.4 | 528 ± 45 | 0.4 ± 0.2 |
| 042574 | 0h3m49.1s | AAE | 1310.3 | 227.8 | 511 ± 57 | 0.5 ± 0.1 |
| 042674 | 18h8m16.9s | AAE | 912.6 | 10.6 | 533 ± 47 | 0.4 ± 0.1 |
| 042974 | 20h4m39.7s | AAE | 2489.4 | 343.8 | 721 ± 65 | 0.3 ± 0.2 |

**Table 2.** *(continued)*

| Event Date | Origin Time † | Recording Station | Epicentral Distance(km) | Back Azimuth | $Q_0$ | $\eta$ |
|---|---|---|---|---|---|---|
| 063074 | 13h26m24.7s | AAE | 777.0 | 6.6 | 563 ± 49 | 0.4 ± 0.1 |
| 090474 | 6h29m16.4s | AAE | 3717.3 | 319.5 | 790 ± 112 | 0.3 ± 0.2 |
| 110880 | 7h54m18.2s | BCAO | 3979.2 | 334.1 | 604 ± 61 | 0.5 ± 0.1 |
| 111080 | 0h1m49.4s | BCAO | 3954.2 | 335.8 | 537 ± 56 | 0.7 ± 0.5 |
| 111780 | 8h29m51.6s | BCAO | 1661.0 | 144.4 | 602 ± 41 | 0.5 ± 0.1 |
| 112080 | 1h38m29.3s | BCAO | 2954.6 | 142.3 | 600 ± 37 | 0.4 ± 0.2 |
| 120780 | 17h37m9.7s | BCAO | 3920.0 | 335.3 | 557 ± 73 | 0.6 ± 0.1 |
| 020181 | 13h19m59.2s | BCAO | 3940.4 | 336.2 | 507 ± 57 | 0.8 ± 0.3 |
| 030481 | 1h58m55.8s | BCAO | 1373.8 | 103.8 | 565 ± 26 | 0.5 ± 0.1 |
| 032381 | 22h28m5.4s | BCAO | 3091.2 | 145.9 | 664 ± 85 | 0.4 ± 0.3 |
| 071981 | 8h7m49.8s | BCAO | 2664.2 | 159.5 | 569 ± 84 | 0.5 ± 0.4 |
| 072381 | 6h21m52.0s | BCAO | 301.7 | 145.4 | 796 ± 22 | 0.3 ± 0.1 |
| 031282 | 4h33m56.8s | BCAO | 1478.6 | 129.2 | 525 ± 40 | 0.5 ± 0.1 |
| 042282 | 4h24m54.3s | BCAO | 1305.5 | 129.7 | 618 ± 120 | 0.5 ± 0.1 |
| 051082 | 12h47m27.9s | BCAO | 2002.0 | 136.3 | 652 ± 24 | 0.5 ± 0.2 |
| 060582 | 19h36m2.3s | BCAO | 1381.5 | 126.7 | 580 ± 59 | 0.6 ± 0.1 |
| 070382 | 23h21m1.2s | BCAO | 1467.5 | 127.8 | 638 ± 55 | 0.4 ± 0.1 |
| 070482 | 2h22m1.4s | BCAO | 1467.3 | 128.0 | 644 ± 50 | 0.4 ± 0.1 |
| 072282 | 9h22m57.9s | BCAO | 1349.3 | 113.5 | 520 ± 45 | 0.6 ± 0.1 |
| 072482 | 3h51m41.6s | BCAO | 1333.1 | 105.1 | 599 ± 51 | 0.6 ± 0.1 |
| 080382 | 12h19m9.2s | BCAO | 1776.8 | 134.8 | 611 ± 49 | 0.6 ± 0.3 |
| 080482 | 1h42m15.3s | BCAO | 3093.5 | 144.5 | 574 ± 16 | 0.5 ± 0.3 |
| 080682 | 21h43m23.7s | BCAO | 2381.8 | 159.9 | 514 ± 48 | 0.5 ± 0.3 |
| 082082 | 12h57m33.3s | BACO | 2599.4 | 34.1 | 653 ± 62 | 0.5 ± 0.2 |
| 082182 | 5h46m1.6s | BCAO | 2392.3 | 160.0 | 675 ± 97 | 0.5 ± 0.2 |
| 092582 | 21h51m27.6s | BCAO | 1776.8 | 132.2 | 665 ± 12 | 0.6 ± 0.1 |
| 110882 | 18h29m47.7s | BCAO | 1770.9 | 153.9 | 513 ± 23 | 0.3 ± 0.2 |
| 111882 | 8h43m19.1s | BCAO | 1474.6 | 125.8 | 574 ± 19 | 0.5 ± 0.2 |
| 120482 | 18h3m45.4s | BCAO | 1991.2 | 134.0 | 758 ± 73 | 0.6 ± 0.2 |
| 120782 | 9h36m3.3s | BCAO | 1807.3 | 134.2 | 654 ± 20 | 0.7 ± 0.3 |
| 122282 | 0h44m50.0s | BCAO | 1089.9 | 117.9 | 657 ± 38 | 0.5 ± 0.1 |
| 122782 | 2h43m9.1s | BCAO | 2162.3 | 121.6 | 570 ± 35 | 0.6 ± 0.1 |
| 011583 | 16h34m7.8s | BCAO | 1366.0 | 108.2 | 527 ± 59 | 0.6 ± 0.2 |
| 011783 | 4h18m16.6s | BCAO | 3092.5 | 145.4 | 698 ± 71 | 0.6 ± 0.2 |
| 020383 | 13h46m2.3s | BCAO | 3299.8 | 30.40 | 811 ± 97 | 0.2 ± 0.4 |
| 022683 | 19h49m19.1s | BCAO | 2121.1 | 115.5 | 651 ± 44 | 0.4 ± 0.1 |
| 110283 | 2h35m12.8s | BCAO | 2088.5 | 112.8 | 593 ± 75 | 0.6 ± 0.2 |
| 011184 | 18h40m29.6s | BCAO | 1568.9 | 138.6 | 768 ± 78 | 0.5 ± 0.5 |
| 011484 | 13h36m10.3s | BCAO | 1686.2 | 139.8 | 413 ± 19 | 0.6 ± 0.3 |
| 083084 | 10h26m49.4s | BCAO | 1694.5 | 141.3 | 599 ± 57 | 0.5 ± 0.2 |
| 101484 | 20h41m17.9s | BCAO | 1277.2 | 148.2 | 396 ± 42 | 0.4 ± 0.2 |
| 103084 | 15h24m7.5s | BCAO | 1162.8 | 132.8 | 530 ± 33 | 0.6 ± 0.1 |
| 111784 | 11h42m45.1s | BCAO | 1668.7 | 141.2 | 614 ± 39 | 0.4 ± 0.3 |
| 022385 | 14h45m35.9s | BCAO | 1864.7 | 132.4 | 646 ± 156 | 0.5 ± 0.5 |
| 022885 | 16h55m47.2s | BCAO | 3063.7 | 30.3 | 797 ± 32 | 0.2 ± 0.1 |
| 052885 | 6h1m32.3s | BCAO | 1699.5 | 127.6 | 587 ± 57 | 0.6 ± 0.4 |
| 062185 | 20h41m4.1s | BCAO | 1673.1 | 141.4 | 401 ± 26 | 0.7 ± 0.3 |
| 062885 | 22h46m19.8s | BCAO | 1381.9 | 123.3 | 544 ± 42 | 0.6 ± 0.2 |
| 090385 | 9h49m22.9s | BCAO | 1323.5 | 116.5 | 430 ± 21 | 0.5 ± 0.2 |
| 011373 | 6h5m42.4s | BUL | 369.7 | 355.9 | 641 ± 53 | 0.4 ± 0.1 |
| 011473 | 13h36m59.8s | BUL | 1480.1 | 7.3 | 454 ± 50 | 0.5 ± 0.1 |
| 030973 | 13h1m46.5s | BUL | 882.7 | 190.0 | 628 ± 49 | 0.4 ± 0.1 |
| 031173 | 10h40m6.2s | BUL | 400.6 | 350.6 | 681 ± 65 | 0.3 ± 0.2 |
| 040873 | 0h28m18.7s | BUL | 1344.6 | 17.1 | 573 ± 55 | 0.5 ± 0.1 |
| 041573 | 13h13m33.4s | BUL | 1443.6 | 7.4 | 560 ± 66 | 0.5 ± 0.1 |
| 041973 | 2h12m12.7s | BUL | 376.5 | 352.7 | 672 ± 57 | 0.5 ± 0.2 |
| 050373 | 2h27m13.0s | BUL | 1367.1 | 19.6 | 545 ± 60 | 0.4 ± 0.1 |
| 050773 | 18h1m2.2s | BUL | 412.8 | 348.9 | 694 ± 68 | 0.3 ± 0.2 |
| 051473 | 15h22m41.2s | BUL | 507.8 | 88.6 | 660 ± 46 | 0.3 ± 0.1 |
| 051473 | 20h16m26.8s | BUL | 1537.5 | 6.0 | 506 ± 63 | 0.4 ± 0.2 |
| 052773 | 9h26m0.7s | BUL | 1239.2 | 30.3 | 533 ± 48 | 0.4 ± 0.1 |
| 053173 | 4h19m35.8s | BUL | 1374.4 | 19.1 | 561 ± 54 | 0.5 ± 0.2 |
| 070773 | 16h4m9.9s | BUL | 2027.8 | 22.6 | 509 ± 79 | 0.5 ± 0.2 |
| 071673 | 18h8m20.0s | BUL | 1223.9 | 30.5 | 598 ± 39 | 0.4 ± 0.1 |
| 072573 | 16h59m39.2s | BUL | 1011.6 | 44.3 | 528 ± 60 | 0.5 ± 0.2 |
| 090173 | 11h23m54.6s | BUL | 894.3 | 327.0 | 759 ± 69 | 0.3 ± 0.1 |
| 090773 | 23h27m50.9s | BUL | 531.2 | 105.8 | 705 ± 64 | 0.3 ± 0.1 |
| 092173 | 11h12m48.8s | BUL | 1606.6 | 36.0 | 563 ± 78 | 0.3 ± 0.2 |
| 121473 | 15h4m10.5s | BUL | 1707.5 | 358.4 | 652 ± 53 | 0.3 ± 0.2 |
| 020474 | 1h29m48.8s | BUL | 388.4 | 353.9 | 714 ± 49 | 0.3 ± 0.1 |
| 021074 | 16h29m26.4s | BUL | 1994.9 | 342.7 | 747 ± 48 | 0.3 ± 0.2 |
| 032174 | 12h17m37.0s | BUL | 686.4 | 189.8 | 643 ± 39 | 0.4 ± 0.1 |
| 042474 | 18h59m53.0s | BUL | 747.3 | 343.1 | 661 ± 45 | 0.4 ± 0.1 |
| 051474 | 6h51m15.4s | BUL | 687.3 | 189.0 | 617 ± 43 | 0.4 ± 0.1 |
| 062474 | 15h12m57.8s | BUL | 691.6 | 191.3 | 649 ± 52 | 0.3 ± 0.1 |
| 062574 | 15h27m32.7s | BUL | 687.1 | 191.6 | 623 ± 55 | 0.4 ± 0.2 |
| 072374 | 14h9m56.0s | BUL | 733.9 | 192.7 | 581 ± 63 | 0.3 ± 0.2 |
| 091774 | 14h30m54.9s | BUL | 1387.8 | 16.1 | 527 ± 67 | 0.5 ± 0.2 |
| 100474 | 17h4m52.6 | BUL | 1122.3 | 33.0 | 633 ± 29 | 0.3 ± 0.1 |
| 101174 | 12h3m43.7s | BUL | 1269.0 | 200.5 | 544 ± 56 | 0.4 ± 0.2 |
| 011373 | 6h5m42.4s | GRM | 1386.3 | 16.5 | 379 ± 31 | 0.5 ± 0.1 |
| 030973 | 13h1m46.5s | GRM | 592.0 | 4.6 | 346 ± 33 | 0.5 ± 0.1 |
| 052473 | 7h15m8.5s | GRM | 2646.4 | 17.8 | 369 ± 41 | 0.5 ± 0.2 |

**Table 2.** (*continued*)

| Event Date | Origin Time † | Recording Station | Epicentral Distance(km) | Back Azimuth | $Q_0$ | $\eta$ |
|---|---|---|---|---|---|---|
| 030973* | 13h1m46.5s | GRM | 735.9 | 5.9 | 381 ± 40 | 0.5 ± 0.1 |
| 022765 | 11h30m0.0s | HLW | 2672.0 | 262.4 | 842 ± 63 | 0.2 ± 0.1 |
| 030573 | 23h59m46.6s | HLW | 336.0 | 135.2 | 659 ± 44 | 0.4 ± 0.1 |
| 022574 | 16h5m15.7s | HLW | 2395.2 | 155.8 | 667 ± 71 | 0.3 ± 0.1 |
| 031774 | 7h31m25.2s | HLW | 1834.6 | 181.6 | 784 ± 72 | 0.3 ± 0.1 |
| 042574 | 0h3m49.1s | *HLW* | 3193.8 | 182.4 | 662 ± 58 | 0.4 ± 0.1 |
| 063074 | 13h26m24.7s | HLW | 1755.5 | 149.0 | 382 ± 25 | 0.6 ± 0.1 |
| 092374 | 19h28m17.2s | HLW | 3857.1 | 213.5 | 780 ± 72 | 0.3 ± 0.1 |
| 020878 | 16h14m38.5s | ICA** | 3400.0 | 78.5 | 646 ± 51 | 0.6 ± 0.1 |
| 060778 | 7h21m21.5s | ICA** | 3015.9 | 42.7 | 757 ± 56 | 0.6 ± 0.1 |
| 120978 | 7h12m52.4s | ICA** | 3859.7 | 56.4 | 746 ± 66 | 0.5 ± 0.1 |
| 121178 | 8h56m36.7s | ICA** | 3017.2 | 9.5 | 804 ± 42 | 0.6 ± 0.1 |
| 101080 | 14h44m52.6s | ICA** | 3359.9 | 10.4 | 608 ± 32 | 0.8 ± 0.2 |
| 101380 | 6h37m39.2s | ICA** | 3365.7 | 10.8 | 676 ± 74 | 0.8 ± 0.2 |
| 120380 | 10h31m20.1s | ICA** | 3376.6 | 10.3 | 651 ± 45 | 0.5 ± 0.1 |
| 111481 | 9h5m29.0s | ICA** | 4438.8 | 60.4 | 768 ± 43 | 0.6 ± 0.1 |
| 091182 | 21h40m12.2s | ICA** | 3379.7 | 11.2 | 681 ± 61 | 0.5 ± 0.1 |
| 093083 | 18h58m14.3s | ICA** | 5321.7 | 79.8 | 565 ± 61 | 0.6 ± 0.1 |
| 031584 | 19h0m37.2s | ICA** | 3341.4 | 21.9 | 701 ± 66 | 0.5 ± 0.1 |
| 070284 | 1h46m58.9s | ICA** | 4683.8 | 59.2 | 662 ± 67 | 0.6 ± 0.1 |
| 010773 | 12h17m12.6s | NAI | 722.3 | 0.4 | 455 ± 49 | 0.5 ± 0.2 |
| 011473 | 13h36m59.8s | NAI | 948.4 | 229.3 | 436 ± 35 | 0.5 ± 0.1 |
| 031173 | 10h40m6.2s | NAI | 1945.5 | 209.2 | 499 ± 40 | 0.4 ± 0.1 |
| 040573 | 2h56m48.0s | NAI | 1940.9 | 209.1 | 507 ± 37 | 0.5 ± 0.2 |
| 040773 | 19h17m38.7s | NAI | 1584.0 | 24.5 | 421 ± 50 | 0.5 ± 0.1 |
| 040873 | 0h28m18.7s | NAI | 946.4 | 212.5 | 409 ± 55 | 0.5 ± 0.1 |
| 041373 | 14h13m56.9s | NAI | 1651.4 | 27.7 | 440 ± 50 | 0.5 ± 0.1 |
| 041573 | 13h13m33.4s | NAI | 974.5 | 227.8 | 419 ± 45 | 0.5 ± 0.1 |
| 041973 | 2h12m12.7s | NAI | 1955.7 | 208.4 | 460 ± 40 | 0.5 ± 0.1 |
| 042273 | 22h3m43.5s | NAI | 848.4 | 312.5 | 403 ± 35 | 0.5 ± 0.1 |
| 050373 | 2h27m13.5s | NAI | 910.6 | 209.3 | 428 ± 29 | 0.5 ± 0.2 |
| 051473 | 15h22m41.2s | NAI | 2097.1 | 189.7 | 457 ± 46 | 0.5 ± 0.1 |
| 051473 | 20h16m26.8s | NAI | 932.8 | 233.3 | 449 ± 31 | 0.5 ± 0.1 |
| 052473 | 7h15m8.5s | NAI | 1056.4 | 198.4 | 435 ± 59 | 0.5 ± 0.2 |
| 070773 | 16h4m9.9s | NAI | 245.8 | 214.8 | 431 ± 48 | 0.5 ± 0.1 |
| 071873 | 19h39m13.0s | NAI | 1126.0 | 193.3 | 420 ± 48 | 0.5 ± 0.2 |
| 090173 | 11h23m54.6s | NAI | 1927.7 | 225.8 | 497 ± 51 | 0.5 ± 0.1 |
| 092173 | 11h12m48.8s | NAI | 767.4 | 177.2 | 430 ± 51 | 0.4 ± 0.2 |
| 120173 | 16h51m14.0s | NAI | 837.4 | 284.6 | 395 ± 34 | 0.5 ± 0.1 |
| 121473 | 15h4m10.5s | NAI | 1028.4 | 248.2 | 441 ± 57 | 0.5 ± 0.2 |
| 121973 | 3h6m58.8s | *NAI* | 3044.6 | 199.7 | 557 ± 60 | 0.4 ± 0.2 |
| 012174 | 15h15m54.0s | NAI | 2896.2 | 198.0 | 513 ± 47 | 0.5 ± 0.1 |
| 020174 | 15h49m29.2s | NAI | 2178.9 | 212.0 | 558 ± 39 | 0.4 ± 0.1 |
| 020474 | 13h16m55.3s | NAI | 1957.0 | 208.8 | 442 ± 51 | 0.5 ± 0.1 |
| 021074 | 16h29m26.4s | NAI | 1506.2 | 263.1 | 471 ± 44 | 0.5 ± 0.2 |
| 021874 | 9h59m45.7s | NAI | 841.5 | 254.9 | 460 ± 39 | 0.5 ± 0.1 |
| 022574 | 16h5m15.7s | NAI | 1278.9 | 16.2 | 443 ± 37 | 0.5 ± 0.2 |
| 031774 | 7h31m25.2s | NAI | 1740.8 | 337.7 | 478 ± 45 | 0.4 ± 0.2 |
| 062474 | 15h12m57.8s | NAI | 2945.5 | 199.5 | 573 ± 47 | 0.4 ± 0.1 |
| 072374 | 14h9m56.0s | NAI | 2990.1 | 199.7 | 581 ± 40 | 0.4 ± 0.1 |
| 011373 | 6h5m42.4s | PRE | 989.9 | 1.1 | 779 ± 67 | 0.3 ± 0.2 |
| 011473 | 13h36m59.8s | PRE | 2101.7 | 6.5 | 612 ± 79 | 0.4 ± 0.2 |
| 022073 | 15h19m51.7s | PRE | 1005.4 | 358.5 | 685 ± 68 | 0.4 ± 0.2 |
| 031173 | 10h40m6.2s | PRE | 1016.4 | 358.9 | 651 ± 79 | 0.4 ± 0.2 |
| 040573 | 2h56m48.0s | PRE | 1019.0 | 359.1 | 742 ± 74 | 0.3 ± 0.1 |
| 041573 | 13h13m33.4s | PRE | 2065.2 | 6.5 | 673 ± 43 | 0.4 ± 0.2 |
| 041973 | 2h12m12.7s | PRE | 994.4 | 359.8 | 782 ± 58 | 0.3 ± 0.1 |
| 050073 | 18h1m2.2s | PRE | 1973.3 | 15.0 | 639 ± 49 | 0.5 ± 0.1 |
| 050873 | 5h22m22.9s | PRE | 983.5 | 358.2 | 772 ± 67 | 0.3 ± 0.1 |
| 051473 | 15h22m41.2s | PRE | 838.4 | 41.2 | 681 ± 45 | 0.4 ± 0.1 |
| 051473 | 20h16m26.8s | PRE | 2159.6 | 5.6 | 623 ± 49 | 0.5 ± 0.1 |
| 052473 | 7h15m8.5s | PRE | 1802.8 | 20.0 | 569 ± 55 | 0.4 ± 0.1 |
| 052773 | 9h26m0.7s | PRE | 1817.9 | 21.8 | 608 ± 47 | 0.5 ± 0.1 |
| 053173 | 4h19m35.8s | PRE | 1981.6 | 14.7 | 645 ± 57 | 0.5 ± 0.1 |
| 071673 | 18h8m20.0s | PRE | 1801.8 | 21.9 | 635 ± 48 | 0.4 ± 0.1 |
| 071873 | 19h39m13.0s | PRE | 1739.7 | 23.4 | 611 ± 57 | 0.4 ± 0.1 |
| 082873 | 22h43m16.7s | PRE | 1912.9 | 9.8 | 623 ± 56 | 0.4 ± 0.2 |
| 090173 | 11h23m54.6s | PRE | 1440.9 | 342.1 | 761 ± 53 | 0.3 ± 0.1 |
| 090773 | 23h27m50.9s | PRE | 730.1 | 49.5 | 632 ± 39 | 0.4 ± 0.1 |
| 110373 | 21h35m44.4s | PRE | 719.3 | 45.9 | 713 ± 51 | 0.4 ± 0.1 |
| 020174 | 15h49m29.2s | PRE | 898.5 | 345.3 | 751 ± 71 | 0.3 ± 0.2 |
| 020474 | 1h29m48.8s | PRE | 1007.2 | 0.2 | 687 ± 56 | 0.3 ± 0.2 |
| 020474 | 13h16m55.3s | PRE | 998.8 | 359.3 | 730 ± 68 | 0.3 ± 0.2 |
| 021074 | 16h29m26.4s | PRE | 2584.5 | 347.6 | 761 ± 51 | 0.3 ± 0.1 |
| 040874 | 6h12m49.2s | PRE | 2377.5 | 21.3 | 545 ± 62 | 0.5 ± 0.2 |
| 042474 | 18h59m53.0s | PRE | 1347.2 | 352.6 | 754 ± 53 | 0.4 ± 0.1 |
| 022765 | 11h30m0.0s | SDB | 4406.6 | 347.7 | 590 ± 61 | 0.5 ± 0.1 |
| 040982 | 2h33m58.7s | SLR | 885.0 | 351.2 | 650 ± 32 | 0.4 ± 0.1 |
| 062582 | 18h0m0.8s | SLR | 288.4 | 217.5 | 475 ± 72 | 0.6 ± 0.1 |
| 070482 | 2h22m1.4s | SLR | 2428.4 | 1.7 | 670 ± 75 | 0.3 ± 0.1 |
| 080482 | 1h42m15.3s | SLR | 1087.7 | 41.6 | 623 ± 66 | 0.5 ± 0.1 |
| 080682 | 21h43m23.7s | SLR | 1124.3 | 347.5 | 625 ± 88 | 0.4 ± 0.1 |
| 081982 | 14h6m13.1s | SLR | 292.0 | 21.3 | 505 ± 72 | 0.5 ± 0.1 |

**Table 2.** (*continued*)

| Event Date | Origin Time † | Recording Station | Epicentral Distance(km) | Back Azimuth | $Q_0$ | $\eta$ |
|---|---|---|---|---|---|---|
| 120482 | 18h3m45.4s | SLR | 1979.4 | 10.3 | 612 ± 70 | 0.4 ± 0.1 |
| 061884 | 10h50m1.1s | SLR | 2021.2 | 359.0 | 708 ± 150 | 0.3 ± 0.1 |
| 082584 | 20h37m49.8s | SLR | 1929.6 | 14.0 | 600 ± 124 | 0.4 ± 0.1 |
| 022385 | 14h45m35.9s | SLR | 2094.2 | 8.2 | 464 ± 48 | 0.6 ± 0.1 |
| 050885 | 11h35m45.7s | SLR | 506.8 | 218.4 | 504 ± 42 | 0.4 ± 0.2 |
| 051485 | 13h24m57.8s | SLR | 2175.1 | 41.9 | 639 ± 83 | 0.4 ± 0.2 |
| 062885 | 7h32m19.9s | SLR | 2158.2 | 41.6 | 623 ± 76 | 0.6 ± 0.3 |
| 011373 | 6h5m42.4s | WIN | 295.0 | 42.4 | 715 ± 53 | 0.3 ± 0.1 |
| 011473 | 13h36m59.8s | WIN | 2207.2 | 40.0 | 648 ± 96 | 0.5 ± 0.2 |
| 020673 | 9h50m41.4s | WIN | 1171.3 | 113.3 | 722 ± 67 | 0.3 ± 0.1 |
| 022073 | 15h19m51.7s | WIN | 1264.8 | 60.8 | 750 ± 78 | 0.3 ± 0.2 |
| 030973 | 13h1m46.5s | WIN | 1124.4 | 124.2 | 680 ± 59 | 0.3 ± 0.1 |
| 031173 | 10h40m6.2s | WIN | 1275.9 | 60.5 | 760 ± 78 | 0.3 ± 0.1 |
| 041573 | 13h13m33.4s | WIN | 2176.3 | 40.5 | 600 ± 57 | 0.5 ± 0.2 |
| 041973 | 2h12m12.7s | WIN | 1278.9 | 61.7 | 680 ± 53 | 0.3 ± 0.2 |
| 050373 | 2h27m13.0s | WIN | 2249.3 | 48.4 | 590 ● 56 | 0.5 ● 0.1 |
| 050873 | 5h22m22.9s | WIN | 1294.4 | 61.5 | 730 ± 68 | 0.3 ± 0.1 |
| 051473 | 15h22m41.4s | WIN | 1669.8 | 83.0 | 580 ± 40 | 0.5 ± 0.1 |
| 051473 | 20h16m26.8s | WIN | 2239.8 | 38.5 | 580 ± 56 | 0.5 ± 0.1 |
| 052473 | 7h15m8.5s | WIN | 2187.9 | 54.4 | 550 ± 51 | 0.5 ± 0.2 |
| 052773 | 7h15m8.5s | WIN | 2229.8 | 55.5 | 580 ± 49 | 0.5 ± 0.1 |
| 053173 | 4h19m35.8s | WIN | 2250.8 | 48.1 | 590 ± 61 | 0.5 ± 0.2 |
| 070773 | 16h4m9.9s | WIN | 2893.6 | 44.5 | 510 ± 52 | 0.6 ± 0.2 |
| 071673 | 18h8m20.0s | WIN | 2217.6 | 55.8 | 580 ± 48 | 0.4 ± 0.1 |
| 071873 | 19h39m13.0s | WIN | 2187.3 | 57.7 | 490 ± 57 | 0.5 ± 0.1 |
| 082873 | 22h43m16.7s | WIN | 2106.2 | 45.3 | 590 ± 54 | 0.5 ± 0.1 |
| 090173 | 11h23m54.6s | WIN | 1234.8 | 35.0 | 690 ± 63 | 0.3 ± 0.2 |
| 090673 | 20h13m35.7s | WIN | 1097.5 | 123.9 | 760 ± 58 | 0.3 ± 0.1 |
| 110373 | 21h35m44.4s | WIN | 1614.4 | 87.3 | 570 ± 52 | 0.5 ± 0.1 |
| 121473 | 15h4m10.5s | WIN | 2280.4 | 31.5 | 550 ± 56 | 0.4 ± 0.1 |
| 020174 | 15h49m29.2s | WIN | 1023.1 | 61.1 | 760 ± 75 | 0.2 ± 0.2 |
| 020474 | 13h16m55.3s | WIN | 1272.6 | 61.3 | 690 ± 48 | 0.3 ± 0.1 |
| 021074 | 16h29m26.4s | WIN | 2265.7 | 16.7 | 540 ± 52 | 0.5 ± 0.1 |
| 040874 | 6h12m49.2s | WIN | 2715.5 | 48.8 | 500 ± 57 | 0.6 ± 0.2 |
| 042674 | 12h18m24.4s | WIN | 1143.9 | 112.2 | 720 ± 57 | 0.2 ± 0.2 |
| 062474 | 15h12m57.8s | WIN | 1060.9 | 114.6 | 690 ± 61 | 0.4 ± 0.1 |
| 072374 | 14h9m56.0s | WIN | 1050.3 | 117.0 | 770 ± 77 | 0.2 ± 0.1 |

† The origin times for the two explosional events dated 10-20-63 and 02-28-65 were given by Bolt (1976). The origin times for all the other events were given in PRE.

* $Q_0$ and $\eta$ listed in this line were estimated from averaging spectral ratios obtained from events 03-09-73, 06-10-73, 08-05-73, 09-06-73, 04-26-74, 05-14-74, 06-24-74.

** ICA denotes the Ivory Coast Array. The averaged spectral ratios collected from all the stations were used to estimate $Q_0$ and $\eta$ for each event.



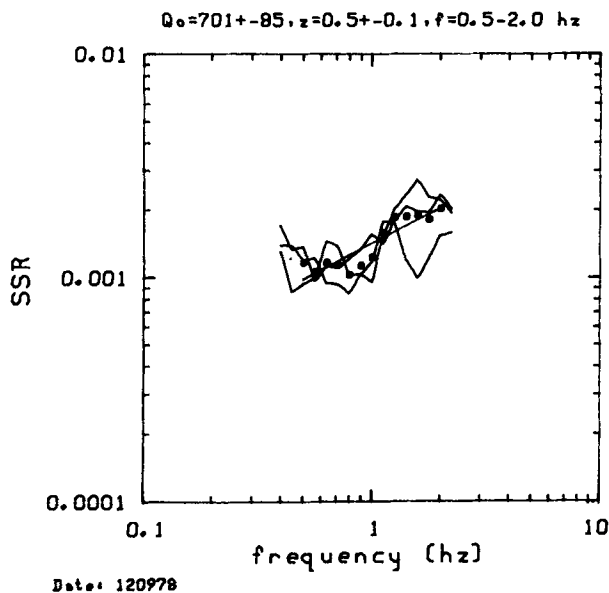$Q_0 = 701 + -85, z = 0.5 + -0.1, f = 0.5 - 2.0$ hz

**Figure 5.** The SSRs calculated from each trace in Fig. 4 (curves), their average (dots) and the result of regression fitting (line) over the average. The resulting $Q_0$ and frequency dependence (denoted by z in this plot) and the frequency band used are given above the figure.

scatterers inland. When part of the ellipse corresponding to $\tau_m$, the centred lapse time of the $m$th window (Xie & Nuttli 1988), is oceanic, equation (A4) of Xie & Nuttli has been used to determine the limits of integration [$\phi_1$ and $\phi_2$ in equation (6) of this paper], to exclude the oceanic crust and to determine the new geometric spreading term, $G_m$. Our assumption of the absence of abnormally strong scattering (or reflection) of $Lg$ waves toward the receiver by the continental boundary is not necessarily valid in all cases. Although there have been some qualitative demonstrations of the possibility of this type of scattering or reflection, quantitative estimates of its effects are not possible at the present time (Kennett 1986). If abnormally strong scattering or reflection does occur at the continental margin our image of lateral variation of $Lg$ coda $Q$ obtained may be biased near those margins.

The assumption of non-transmissibility at continental margins allows us to exclude any oceanic crust in the scattering ellipse in the $Lg$ coda $Q$ analysis. Fig. 6 shows the pattern of coda sampling area corresponding to our data set. These areas are bounded roughly by complete ellipses corresponding to $\tau_{max}$ (equations 9 and 10) but some are truncated by the continental margin.

The density of coverage of these coda sampling areas decreases from south to north. Southern Africa has the densest coda sampling area coverage whereas northern
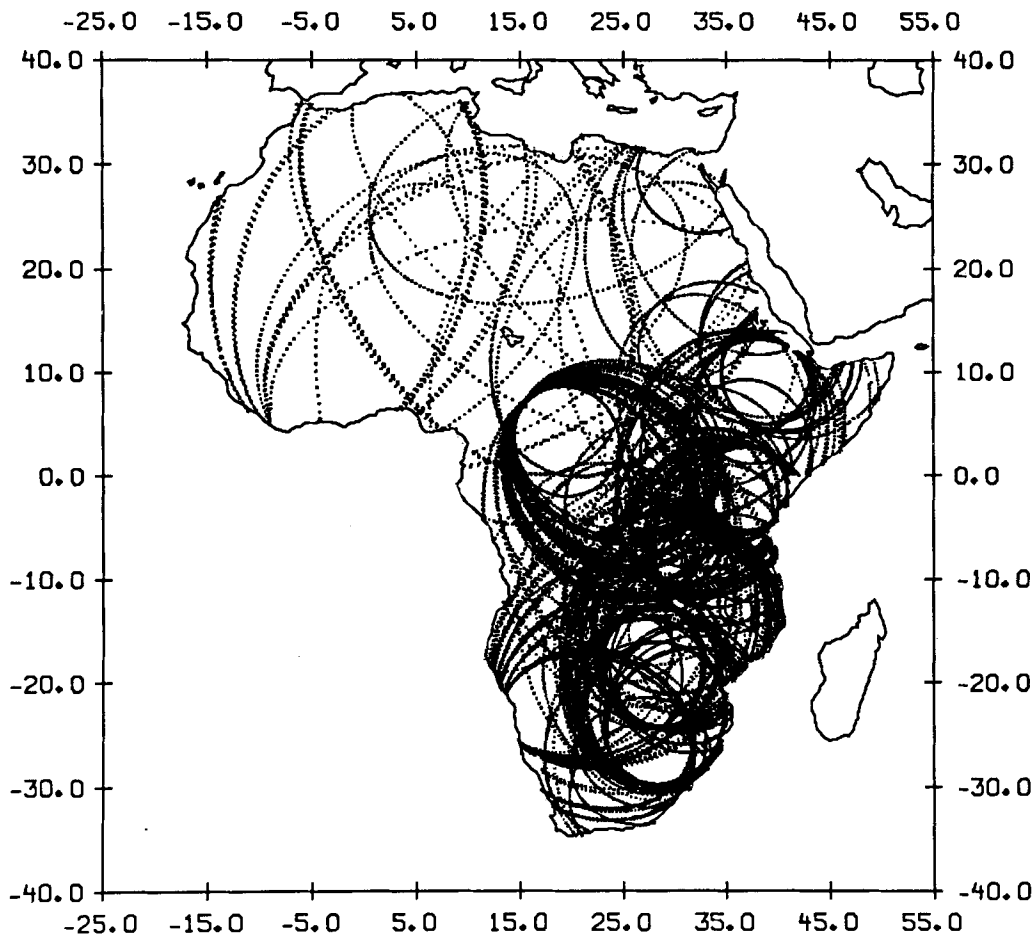
**Figure 6.** Sampling pattern of $Lg$ coda used in this study. Each record of $Lg$ coda is assumed to sample an elliptical area corresponding to the maximum lapse time used in the analysis. When the continental boundary is encountered we assume it is a barrier to the $Lg$ wave and therefore the sampling area is bounded by this boundary, instead of being bounded by the corresponding segment of the ellipse which extends into the ocean.

Africa has the sparsest. For each of the records, the SSR method was applied to obtain a single-trace measurement of $Q_0$ and $\eta$. Examples of the SSR analysis may be found in Xie & Nuttli (1988) and in Figs 3 and 5 of this paper. Most data provide information in the frequency band between 0.5 and 2.0 Hz but digital GDSN data sometimes has high-frequency cut-offs that are higher than 2.0 Hz. Occasionally, when large-amplitude fundamental-mode waves distort coda signal at lower frequencies, we use slightly higher low cut-off values. The results of single-trace determinations of $Q_0$ and $\eta$, together with the sample standard error (s.s.e.), are listed in Table 2. The s.s.e. values of $Q_0$ are almost all within 15 per cent of $Q_0$ and the s.s.e. values of $\eta$ are mostly within 0.2. This is consistent with the stochastic model mentioned in Section 2.1 of this paper.

## 4   LATERAL VARIATIONS OF $Lg$ CODA $Q$

The back projection method in Section 2.3 is applied to image lateral variations of $Lg$ coda $Q$ in continental Africa. We have divided the whole area into 282 grids with widths $W_{EW}$ and $W_{NS}$ equal to $3°$ in latitude and longitude, respectively. The latitudes and longitudes of the centres of the grids span the area between $31.5°S$, $34.5°N$ and $14.5°W$,

$48.5°E$. To find the area sampled by each coda trace we first found the corresponding ellipse in a 2-D Cartesian coordinate system, and projected this ellipse onto the surface of the Earth. Strictly speaking, on a surface with non-zero curvature, an isocron of scatterers corresponding to coda waves received at a constant lapse time is not an ellipse but a more complicated curve. However, we have found that when the axes of ellipses are shorter than approximately 2200 km the difference between the isocron obtained considering the Earth's curvature and the ellipse defined in a Cartesian system without considering the Earth's curvature differs by less than 2 per cent. Since $G_m$ corresponding to an isocron when the Earth's curvature is considered does not have a closed-form solution and since all but a few ellipses in this study have major axes longer than 2200 km, we have ignored the effect of the Earth's curvature on $Q$ imaging.

### 4.1   Lateral variation of $Q_0$

To use the iterative back projection method in Section 2.3 to image lateral variations of $Lg$ coda $Q_0$, we have used a starting model of $Q_m^0 = 600$, $m = 1, 2, \ldots, N_g$ for all of continental Africa. This starting model is roughly the average of all of the single-trace measurements of $Q_0$ (Table
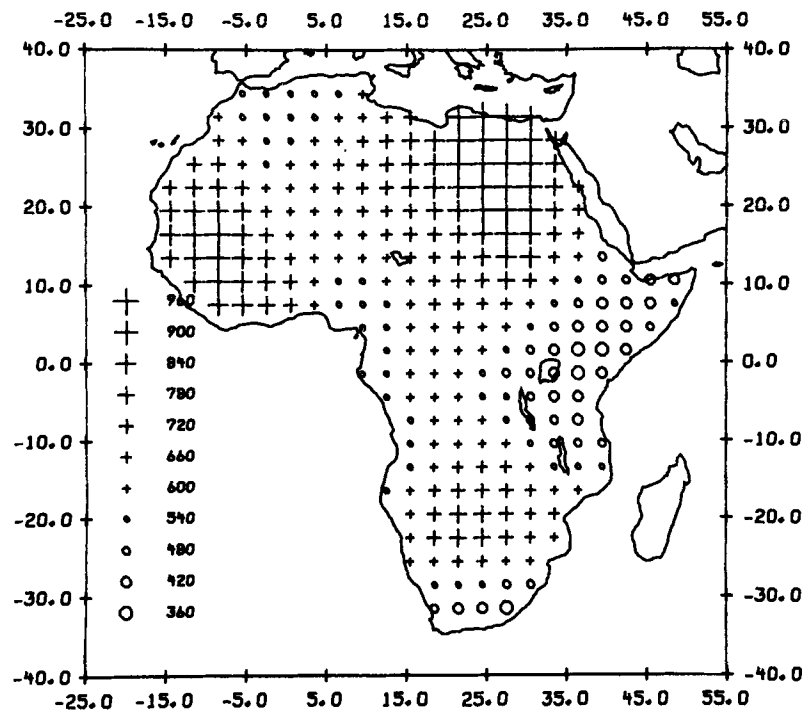
**Figure 7.** *Lg* coda $Q_0$ continental Africa obtained in this study. Circles represent numbers smaller than 570 and crosses represent numbers larger than 570.

2). Single-trace measurements of $Q_0$ were then used as $\overline{Q_n}$ in Section 2.3 to calculate the residuals in the iteration. The stopping criteria, $i_{max}$ and $\delta$, defined by equations (15) and (16), were chosen to be 20 and $10^{-5}$, respectively. The latter criterion was satisfied after 14 iterations. The whole computational process, including calculation of $s_{mn}$ values, took less than 90 min and less than 25 min of CPU time on a Masscomp MC745 and a Ridge-34 minicomputer, respectively. The variance reduction achieved was 95 per cent. After 15 iterations the left-hand side of (16) started to increase slightly, probably due to the accumulation of computer round-off errors. The resulting $Q$ model did not vary significantly after the 14th iteration. Fig. 7 shows the resulting distribution of $Q_0$ in continental Africa. Circles represent $Q_0$ values lower than 570 and crosses represent $Q_0$ values higher than 570. Each symbol represents a $Q_0$ interval of 60, e.g. the smallest circle represents a $Q_0$ value between 510 and 570. The lateral variation of $Q_0$ is rather smooth, indicating that only large-scale variations of $Q_0$ are preserved. Low $Q_0$ values are most apparent in the East African Rift zone and the Cameroon rift (or the Cameroon volcanic line, cf. Moreau *et al.* 1987). Previous single-path observations of the direct *Lg* phase travelling through segments of the East African Rift also indicate low $Q$ values in that region (Gumper & Pomeroy 1970). Low $Q_0$ values also occur near the southern and northern margins of Africa, where the Cape Fold Mountains and Atlas Mountains are located (Fig. 1). High $Q_0$ values occur in central southern Africa where the Congo craton and Kalahari Craton are located, in northwestern Africa where the west Africa craton is located (Clifford 1970; Cahen *et al.* 1984), and in northeastern Africa. The latter area contains the highest mapped $Q_0$ values. Although this region has undergone a complicated tectonic history (Cahen *et al.*

1984), it has not been affected by either large-scale orogeny or volcanic activity for about the last 550 million years and some basement outcrops in this area are dated at ages greater than two billion years (Klerkx 1980).

## 4.2 Lateral variation of $\eta$

Imaging the lateral variation of frequency dependence, $\eta$, requires another procedure. First, we obtained $Q_0$ and $\eta$ for each coda record using the SSR method. This allowed us to calculate single-trace measurements of $Q$ at a frequency other than 1 Hz, say at 3 Hz. These single-trace measurements were then used as $\overline{Q_n}$ in equations (11) and (12) to calculate $Q_m$ values at 3 Hz for each of the $m$ grids, $m = 1, 2, \ldots, N_g$. Finally, using $Q_m$ for each grid calculated at 1 Hz (Section 4.1) and 3 Hz and assuming exponential frequency dependence of $Q$, we calculate $\eta$ for the same grid using the relationship

$$\eta = \frac{1}{\ln 3} \ln \left[ \frac{Q(f)|_{f=3\text{Hz}}}{Q_0} \right]. \tag{17}$$

Fig. 8 shows the resulting lateral variation of $\eta$ in continental Africa. In southern Africa, the frequency dependence is relatively uniform (between 0.3 and 0.5), but is slightly lower (around 0.2–0.3) in central southern Africa, than near the southern margin. $\eta$ is about 0.5 in the region of the East African Rift system. The areas where $\eta$ values are slightly higher in southern Africa are also areas where $Q_0$ is lower (Fig. 7). Near the equator in central Africa (between 10°S and 10°N), $\eta$ is very uniformly distributed, being about 0.5 inland and about 0.6 in coastal areas. In northern Africa $\eta$ exhibits significant lateral variations. Even if the extreme values near the western and northeastern margins are ignored (because sampling

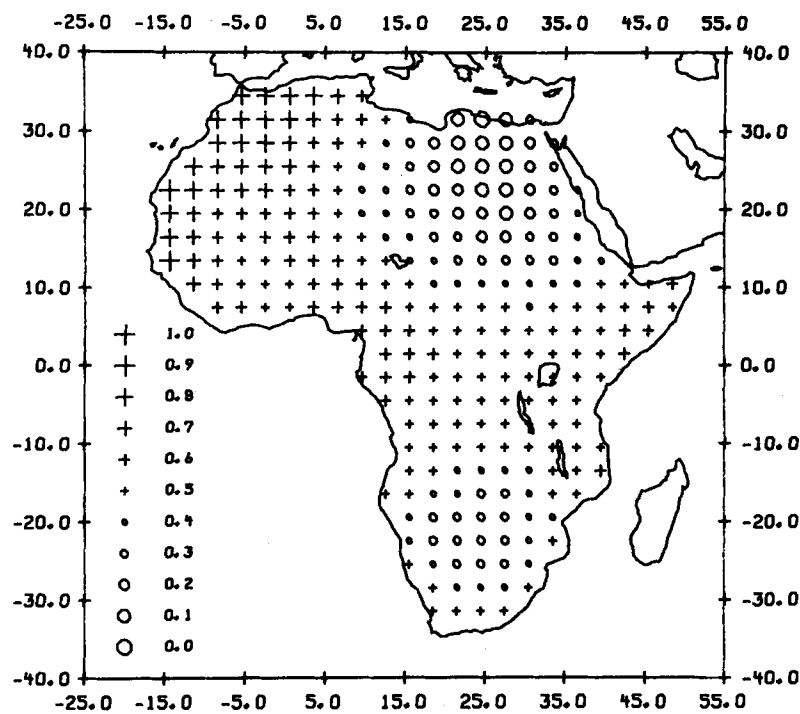**Figure 8.** Frequency dependence ($\eta$) of *Lg* coda *Q* (in the vicinity of 1 Hz) in Africa. Circles represent $\eta$ values smaller than 0.45 and crosses represent $\eta$ values larger than 0.45.

coverage is poor), there is still a large change in $\eta$ from about 0.8 in the West African shield to about 0.1 in the northeastern Africa even though $Q_0$ is high in both regions. Our images of lateral variation of $\eta$ and $Q_0$ do not therefore suggest a systematic correlation between $Q_0$ and $\eta$ throughout the whole continent. If northwestern Africa (where the west African shield is located) is ignored, however, then $\eta$ appears to decrease as $Q_0$ increases. This tendency is most easily seen in northeastern africa and southern Africa. Nuttli (1988) suggested that this relation is generally true throughout the world.

## 5   RESOLUTION AND ERROR

The imaging of *Lg* coda *Q* variations is inherently limited because of the trade-off between the stability and the spatial resolving power (Section 2.2). For this reason it is important that any study of *Lg* coda *Q* variations include an analysis of resolution and error. We have calculated the p.s.f. defined in Section 2.3 for 12 grids (Fig. 9a–g) to estimate the resolving power at the locations where these grids are centred. These locations include: 31.5°S, 24.5°E (b); 28.5°S, 18.5°E (c); 19.5°S, 30.5°E (d); 13.5°S, 24.5°E (a); 13.5°S, 24.5°E (d); 1.5°N, 30.5°E (b); 4.5°N, 21.5°E (f); 7.5°N, 39.5°E (g); 13.5°N, 39.5°E (e); 19.5°N, 3.5°E (d); 19.5°N, 18.5°E (c); 19.5°N, 33.5°E (a). All of the p.s.f. determinations were normalized such that the maximum values are unity. In general, the degree of spreading of p.s.f.'s increases from south to north. This is to be expected since the coda sampling areas are relatively dense in southern Africa and are less dense toward the north (Fig. 6). The p.s.f. plots in Fig. 9(a)–(d) show that in southern Africa the lateral variation of *Lg* coda *Q* is resolvable to spatial wavelengths of between 6° and 20°. Slightly lower

resolving power is obtained in the central part of Africa where the degree of spreading of p.s.f. plots is as low as 12° at 7.5°N and 39.5°E (Fig. 9g) and increases to between 15° and 24° further to the west (Fig. 9b and f). In the north the resolving power decreases drastically, except for some points close to continental margin where resolution spreading is still very low (around 12° to 15°, see Fig. 9a and 9e). For example, at 19.5°N, 18.5°E (Fig. 9c) and 19.5°N, 3.5°E (Fig. 9d) we cannot determine the lateral variation of *Lg* coda *Q* with confidence for spatial wavelengths of less than between 24° and 33°. In summary, the spatial wavelengths of lateral variation in *Lg* coda *Q* that are resolvable range from about 10° in southern Africa to 30° in northern Africa.

It is interesting to compare our resolution in imaging lateral variation in *Lg* coda *Q* to the resolution of 2-D surface wave velocity tomography. Several authors have conducted studies of lateral variations of long-period surface wave phase and/or group velocities in recent years. Suetsugu & Nakanishi (1985), Montagner (1986) and Hadiouche & Jobert (1988) mapped lateral variations of surface wave dispersion in the Pacific Ocean, the Indian Ocean and Africa, respectively, using data at periods between a few seconds and a few hundred seconds. In all these studies the spatial resolving power was generally limited to wavelengths of 15° to 20° or more. Resolving power in some cases was locally limited to 40° for situations where the ray coverage was poor (Suetsugu & Nakanishi 1985). Therefore the resolving power in this study using *Lg* coda waves at frequencies between roughly 0.5 and 2.0 Hz is comparable to that achievable in surface wave tomography at longer periods. This is somewhat surprising since surface wave tomography uses direct paths whereas imaging of lateral variations in the *Lg* coda *Q* uses scattered waves,
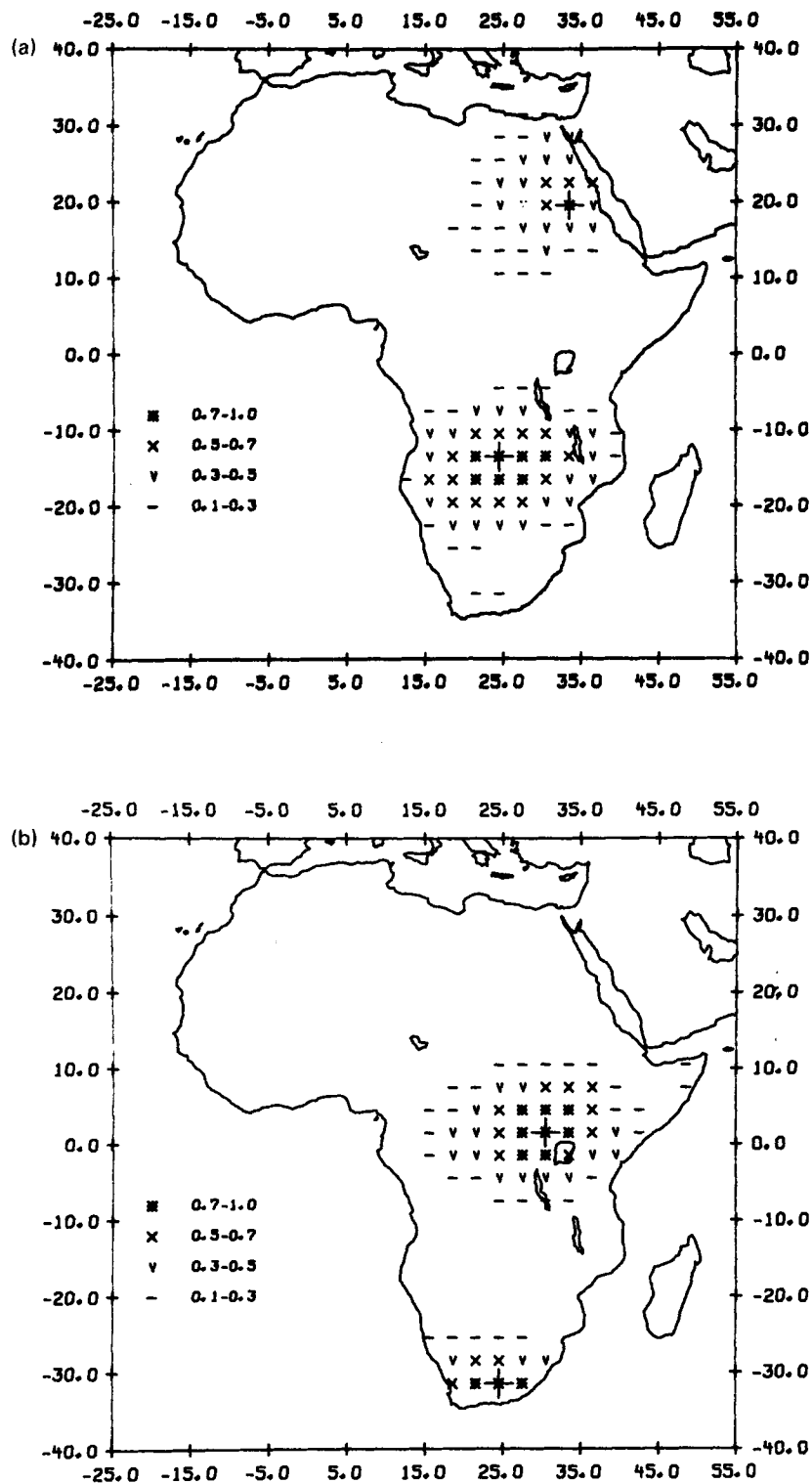
**Figure 9.** (a) Point spreading function (p.s.f.) plots for grids centred at 13.5°S, 24.5°E and 19.5°N, 33.5°E. The p.s.f. plots have been normalized such that the maximum value is unity. The centre of each grid is marked by a large cross. (b) p.s.f. plots for grids centred at 31.5°S, 24.5°E and 1.5°N, 30.5°E. (c) p.s.f. plots for grids centred at 28.5°S, 18.5°E and 19.5°N, 18.5°E. (d) p.s.f. plots for grids centred at 19.5°S, 30.5°E and 19.5°N, 3.5°E. (e) p.s.f. plot for the grid centred at 13.5°N, 39.5°E. (f) p.s.f. plot for the grid centred at 4.5°N, 21.5°E. (g) p.s.f. plot for the grid centred at 7.5°S, 39.5°E.
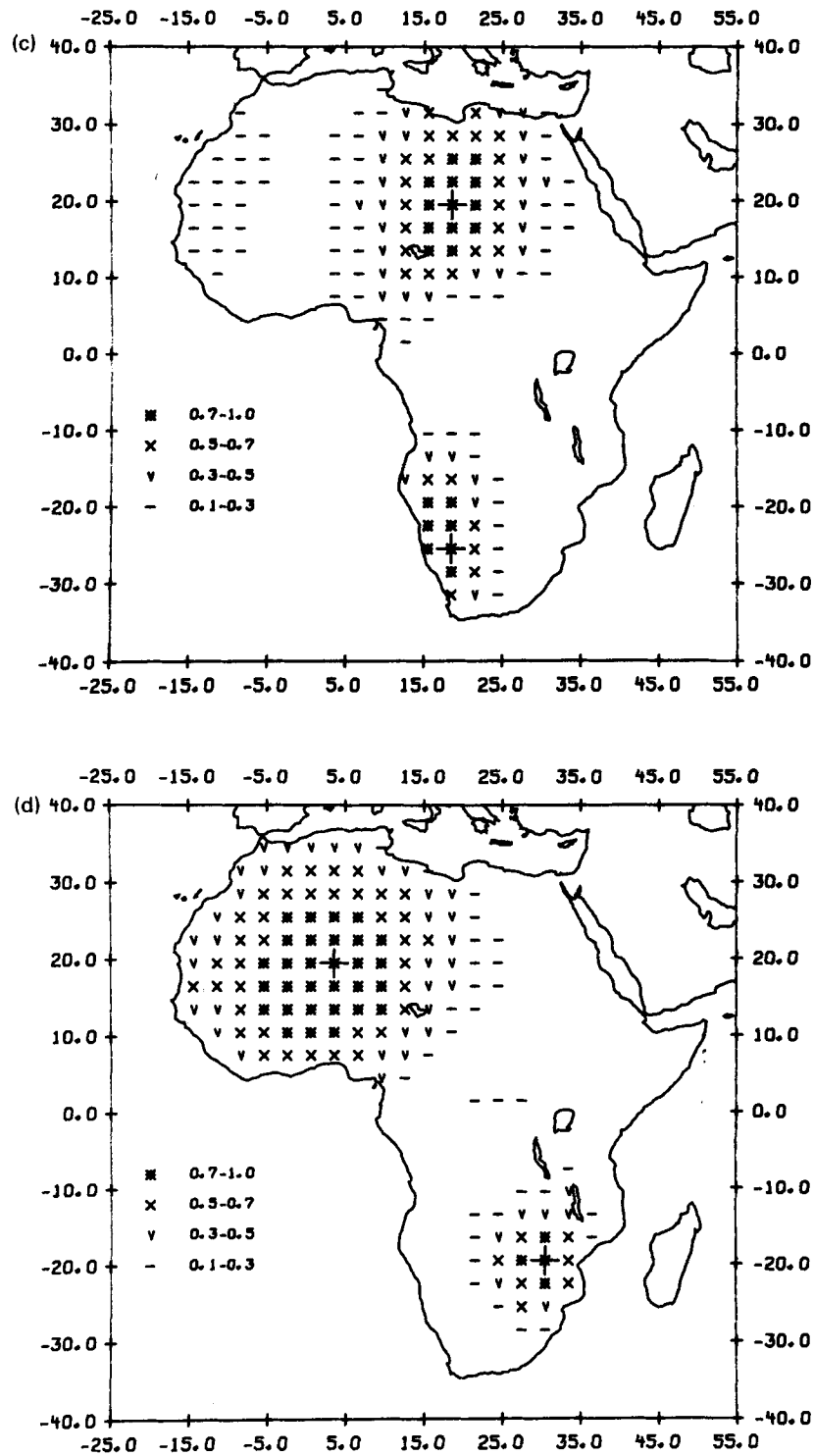
**Figure 9.** (*Continued*)

thus requiring smoothing over broader areas. A closer look at this comparison suggested that the resolving power of surface-wave tomography is limited by gaps between ray paths which are typically about 20°. The smoothing techniques used in surface-wave tomography remove these gaps in the inverted velocity image at the cost of resolution. The limitations in resolution in the present study are, however, largely due to the random nature of coda data itself (Section 2.2). Moreover the $Q$ image may be subjected

to greater systematic errors in the single-trace measurements of $Q$ and in their spatial interpretation than are velocity images from surface waves.

The effect of the random error in single trace measurements of $Lg$ coda $Q$ on the image of lateral variations in $Q$ was estimated empirically using the method described in Section 2.3. Five tests were run to estimate the error in the image of $Q_0$ and $\eta$. In each of the five tests we first constructed two noise, or error series. The absolute
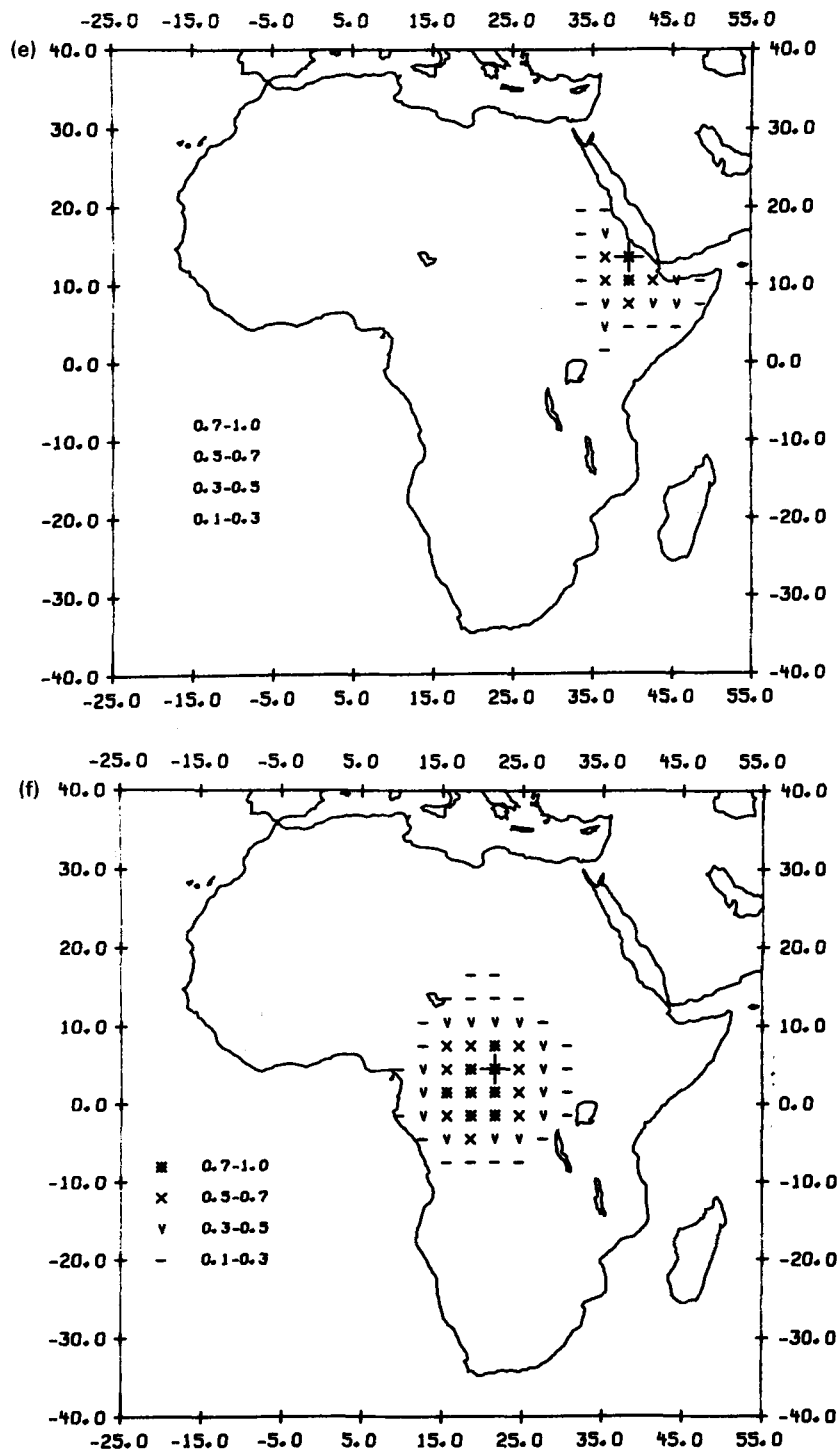
**Figure 9.** (*Continued*)

values of the $n$th terms of the first and the second series equal the sample standard errors in $Q_0$ and $\eta$ calculated from the $n$th coda seismogram, respectively. The signs of the $n$th term of both noise series were randomly generated by a random binary generator. The $n$th terms of the two noise series were than added to the $n$th $Q_0$ and $\eta$ measurements to construct a new synthetic set of $Q_0$ and $\eta$ values. The new sets of synthetic $Q_0$ and $\eta$ values were then inverted using the back projection method to obtain $Q_0$ and $\eta$ for all of the grids. The differences between the $Q_0$ and $\eta$

values for the new image and the original image were then calculated and stored at the end of each test. After all five tests, the absolute values of the five differences in $Q_0$ and $\eta$ for each grid were averaged. The averaged values thus obtained gave empirical estimates of absolute error in the imaged $Q_0$ and $\eta$ values. Figs 10 and 11 give the estimated errors in $Q_0$ and $\eta$, respectively. The errors in $Q_0$ are small (less than 60) throughout most of Africa. Errors are higher, however, in western Africa and northeastern Africa, where the $Q_0$ values are high (Fig. 7). Since the relative error in
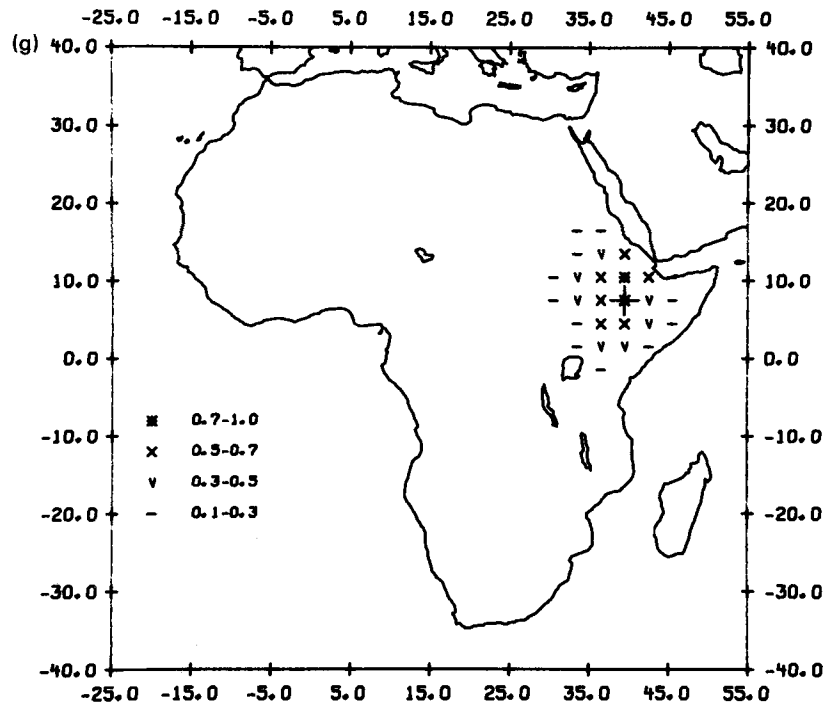
**Figure 9.** (*Continued*)

$Q_0$ tends to have a stochastic distribution (Xie & Nuttli 1988), the increased error in western and northeastern Africa must be partly due to the high $Q_0$ values. The second reason for these increased errors is the poor spatial coverage, especially along the western margin of the continent where the estimated error is as high as 300. The estimated error in $\eta$ is small (0.0–0.1) throughout most of interior Africa and is generally higher at the margins. The error in $\eta$ at the northern margin is typically between 0.3 and 0.4, and is 0.5 in the region of the western margin where sampling is very poor. These calculations indicate that the errors in both $Q_0$ and $\eta$ are inversely related to the density of the coda sampling area.
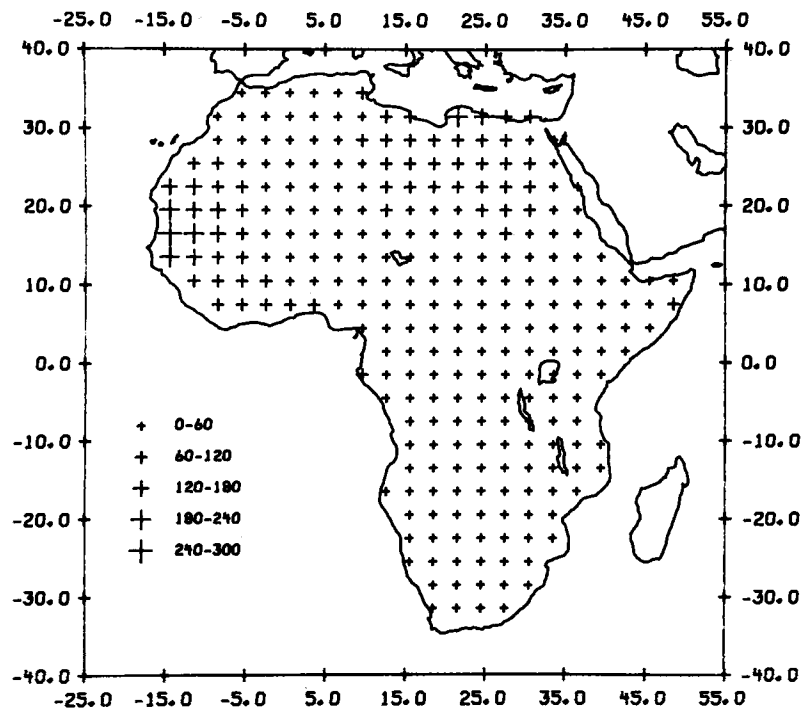


**Figure 10.** Error distribution in the image of lateral variation in $Q_0$ on continental Africa. The error is tested empirically, based on the sample standard error in the $Q_0$ and $\eta$ values calculated from real data and the psuedo-random sign generators. See text for details.
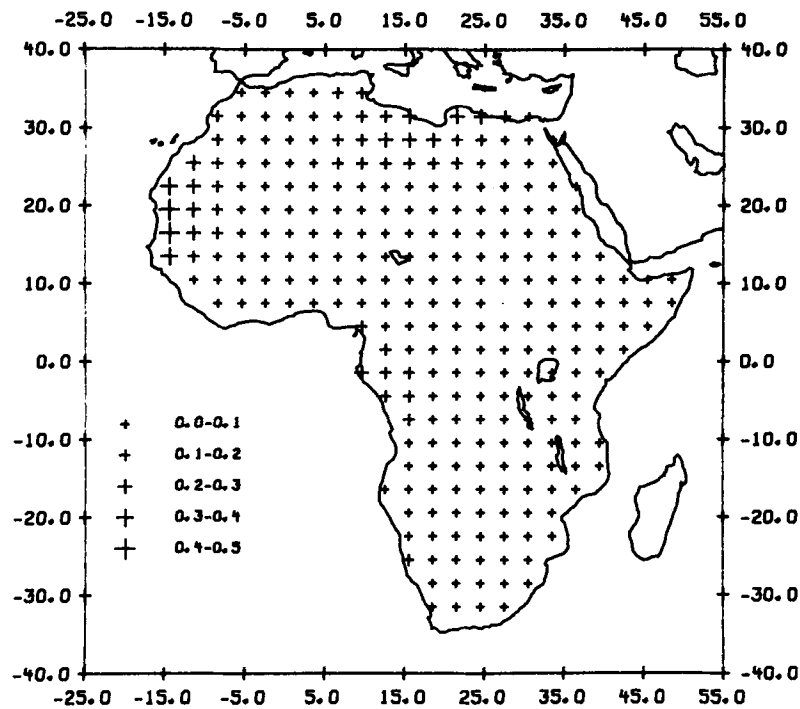
**Figure 11.** Error distribution in the image of lateral variation in $\eta$ on continental Africa. The error is tested empirically, in the same manner as that described in Fig. 10.

## 6 RELATION OF $Q$ VALUES TO GEOLOGICAL FEATURES

The map of $Q_0$ values in Fig. 7 exhibits broad regional variations of $Q_0$ values ranging between about 960 and about 360. The higher values are similar to those found in other stable regions of the world. Since almost all of Africa has been stable for the past 500 million years (Clifford 1970; Cahen *et al.* 1984), we might expect that high $Q$ values would be typical of most of the continent. It is therefore interesting to speculate on the mechanism for the regions of low $Q$ which are observed.

The most obvious region of high attenuation (low $Q$) occurs in eastern Africa and correlates well with the east African Rift system (Fig. 1). This is a region which has been subjected to extensive Cenozoic volcanism and is characterized by $Lg$ coda $Q_0$ values as low as 360. Although these values are lower than those for most of Africa, they are not as low as those found throughout much of the western United States where Cenozoic volcanism has occurred (Singh & Herrmann 1983). The values in Fig. 7 are, however, averages over broad regions including rift areas as well as areas where volcanism has not occurred. It is possible that our results are averages of lower values occurring in the immediate vicinity of the rifts and higher values occurring between and outside the arms of the rifts.

The low $Q$ values in the region of the East African Rift system can be explained as resulting ultimately from higher than normal temperatures in the crust. Morgan (1982) reported a pattern of heat flow values in which high values (up to 98 mW m$^{-2}$) occur on the rift floor and lower values (57 mW m$^{-2}$) occur on the flanks. Mitchell (1975, 1980) proposed that such higher temperatures caused enhanced

levels of hydrothermal fluids in the crust; thus low values of crustal $Q$ can be explained by fluid flow through cracks and connected pore space in the crust by mechanisms such as those proposed by Winkler & Nur (1979) and O'Connell & Budianski (1977).

The Cameroon line running northeastward from the coast in west-central Africa appears to be characterized by relatively low values of $Q_0$ (about 540). This region is also the site of Cenozoic volcanism, so can be expected to have higher than normal heat flow. Its extent, however, is smaller and reductions in $Q$ are less severe than in the East African Rift system.

The lowest values of $Q$ outside the East African Rift system lie in the region of the Cape Fold Belt in southernmost Africa. Orogenic activity occurred there over the time span from middle Palaeozoic to early Mesozoic (Clifford 1970). Although the low $Lg$ coda $Q$ values in southern Africa appear to be associated with the Cape Fold Belt, the mechanism for the low values is uncertain. They can be explained either by reductions of intrinsic $Q$ produced by interstitial fluids (Mitchell 1975, 1980) or by disruption of the crustal wave guide caused by severe topography and fluctuating thickness of sediments. Higher than normal heat flow values in much of southern Africa (Jones 1988), however, may be suggestive of the former mechanism.

Low $Q_0$ values (about 540) in northwestern Africa correlate geographically with the Atlas Mountains. These mountains are the result of the most recent orogenic activity in Africa, thus low $Q$ values might be expected to occur in that region.

A broad band of low $Q_0$ values (about 600) runs in a southeasterly direction from a portion of the Atlas

Mountains near Gibraltar, crosses the Cameroon line, and continues southeastward to about 10°D latitude. Except near the Cameroon line and Atlas mountains, these low values cannot be related to any recent orogenic or volcanic activity in Africa. They do, however, correlate with a broad region of Mesozoic and younger sediments which is mapped in that region (Choubert & Faure-Muret 1971). Mitchell & Hwang (1987) showed that all of the regional variations of *Lg* coda *Q* in the stable portions of the central United States can easily be explained by high attenuation caused by accumulations of sediments of Mesozoic age and younger.

In summary, *Q* values throughout most of Africa are high or relatively high and are consistent with values obtained in other stable regions of the world. Low values occur in regions of Cenozoic volcanism and in the two small regions (Cape Fold Belt and Atlas Mountains) where orogenic activity has occurred as recently as the Mesozoic Era. Somewhat low values appear to be associated with broad regions of sedimentary cover of Mesozoic age.

## 7  CONCLUSIONS AND DISCUSSION

Taking advantage of recent developments in both more stable single-trace measurements of *Lg* coda *Q* and in the rapid evolution of seismic tomography, a computerized back-projection method is proposed to image large-scale lateral variation of *Lg* coda *Q*. Several major differences can be recognized between this method and the earlier contouring methods used by various authors. First, this method assumes that each *Lg* coda time series samples an area rather than a spatial point, thus better approximating the real coda sampling process. Second, this method is fully computerized and quantitative, yet requires very small computer memory and time. Even when a major continental area is studied, a minicomputer is more than adequate. This new method also allows quantitative estimates of resolution and error. The analysis of resolution is especially important in coda *Q* inversion because of the inherent randomness of signal which limits resolution.

We have collected a large amount of digital and digitized *Lg* coda data from continental Africa. Applying the back-projection method to this data base, we find that the lateral variation of $Q_0$ (*Q* at 1 Hz) correlates well with major tectonic features. The Cape Fold Belt, the Atlas Mountains, the East African rift and Cameroon rift (or the Cameroon volcanic line) are characterized by relatively low *Q* values whereas the shields in southern and western Africa are characterized by high *Q* values. Northeastern Africa, another stable region, also has high *Q* values. In most regions the frequency dependence, $\eta$, increases with decreasing values of $Q_0$. However, higher $\eta$ values were also found in the West Africa Shield where $Q_0$ is high. It is possible that larger errors or poorer resolution in western Africa has caused this inconsistency.

A quantitative resolution analysis indicates that the resolving power of the *Lg* coda *Q* image in continental Africa is limited to spatial variations with wavelengths ranging between 10° and 30°. This is comparable to the resolving power of long-period surface-wave tomography applied in earlier studies. The resolution is best in southern Africa where the coda sampling area is densest. The error analysis shows that the errors in the images of both $Q_0$ and

$\eta$ inversely correlate with the density of coda sampling area. For most of interior Africa the error in the imaged $Q_0$ is lower than 60 and the error in the imaged $\eta$ is less than 0.2. The largest errors occur near the northern and western margins of Africa.

Out knowledge of both the distribution and characteristics of scatterers is limited, and the quantity of available data is still very small. These limitations currently prevent us from obtaining detailed knowledge of the physical process which governs the generation and propagation of the *Lg* coda wave. Our assumption that a single-trace measurement of *Lg* coda uniformly samples an elliptical area limits the resolving power of this imaging process. A non-linear approach may overcome this limitation (Xie & Mitchell 1988), but errors in the forward modelling procedure and in the final image are likely to be larger. A non-linear approach will also greatly increase computer time and will require a very large amount of computer storage. For the present, therefore, it is preferable and more convenient to have lower resolving power than to attempt to achieve greater detail with a non-linear approach. Future work should include systematic studies of more detailed interpretations of the dynamic properties and stochastic characteristics of *Lg* and *Lg* coda, which, if combined with an increased data base, should enable us to improve the resolution and quality of the *Q* image.

## ACKNOWLEDGMENTS

## REFERENCES

Aki, K. & Chouet, B., 1975. Origin of coda waves: source, attenuation and scattering effects, *J. geophys. Res.*, **80**, 3322–3342.

Backus, G. & Gilbert, F., 1970. Uniqueness in the inversion of inaccurate gross earth data, *Phil. Trans. R. Soc. Lond.*, **266**, 123–192.

Bolt, B. A., 1976. *Nuclear Explosions and Earthquakes, the Parted Veil*, W. H. Freeman, San Francisco.

Cahan, L., Snelling, N. J., Delhal, J. & Vail, J. R., 1984. *The Geology and Evolution of Africa*, Clarendon Press, Oxford.

Campillo, M., 1987. *Lg* wave propagation in a laterally varying crust and the distribution of the apparent quality factor in central France, *J. geophys. Res.*, **92**, 12 604–12 614.

Cheng, C. C. & Mitchell, B. J., 1981. Crustal *Q* structure in the United States from multi-mode surface waves, *Bull. seism. Soc. Am.*, **71**, 161–181.

Choubert, par, G. & Faure-Muret, A., 1971. Grand bassins sedimentarires de L'Afrique occidentale, in *Tectonics of Africa*, Unesco, Paris.

Clifford, T. N., 1970. The structural framework of Africa, in *African Magmatism and Tectonics*, eds Clifford, T. N. & Gass, I. G., Oliver & Boyd, Edinburgh.

Der, Z., Marshall, M. E., O'Donnell, A. & McElfresh, T. W., 1984. Spatial coherence structure and attenuation the *Lg* phase, site effects, and interpretation of the *Lg* coda, *Bull. seism. Soc. Am.*, **74**, 1125–1148.

Dines, K. A. & Lytle, R. J. 1979. Computerized geophysical tomography, *Proc. IEEE*, **67**, 1065–1073.

Dott, R. H. & Batten R. L., 1971. *Evolution of the Earth*, McGraw-Hill, New York.

Gordon, R., 1974. A tutorial on ART, *IEEE Trans. Nucl. Sci.*, **NS-21**, 78–93.

Gumper, F. & Pomeroy, P. W., 1970. Seismic wave velocities and earth structure on the African continent, *Bull. seism. Soc. Am.*, **60**, 651–668.

Hadiouche, O. & Jobert, N., 1988. Geographical distribution of surface wave velocities and 3-D upper mantle structure in Africa, *Geophys. J.*, **95**, 87–110.

Herrmann, R. B., 1980. *Q* estimates using the coda of local earthquakes, *Bull. seism. Soc. Am.*, **70**, 447–468.

Humphreys, E. & Clayton, R. W., 1988. Adaptation of back projection tomography to seismic travel time problems, *J. geophys. Res.*, **93**, 1073–1086.

Jin, A. & Aki, K., 1988. Spatial and temporal correlation between coda *Q* and seismicity in China, *Bull. seism. Soc. Am.*, **78**, 741–769.

Jones, M. Q. W., 1988. Heat flow in the Witwatersand Basin and Environs and its significance for the South African Shield geotherm and lithospheric thickness, *J. geophys. Res.*, **93**, 3243–3260.

Kennett, B. L. N., 1984. Guided wave propagation in laterally varying media—I. Theoretical development, *Geophys. J. R. astr. Soc.*, **79**, 235–255.

Kennett, B. L. N., 1986. *Lg* waves and structural boundaries, *Bull. seism. Soc. Am.*, **76**, 1133–1141.

Klerkx, J., 1980. Age and metamorphic evolution of the basement complex around Jadal al'Awaynat, in *The Geology of Libya, Part III*, pp. 901–906, eds Salem, M. J. & Busrewil, Academic Press, London.

Knopoff, L., Schwab, F. & Kausel, E., 1973. Interpretation of *Lg*, *Geophys. J. R. astr. Soc.*, **33**, 389–404.

Kopnichev, Y. F., 1980. Statistical models for the generation of coda and short-period *Lg*-phases and the results of their joint interpretation, *Izv. Akad. Nauk USSR. Earth Phys.*, **16**, 99–108.

McMechan, G. A., 1983. Seismic tomography in boreholes, *Geophys. J. R. astr. Soc.*, **74**, 601–612.

Mitchell, B. J., 1975. Regional Rayleigh wave attenuation in North America, *J. geophys. Res.*, **80**, 4904–4916.

Mitchell, B. J., 1980. Frequency dependence of shear wave internal friction in the continental crust of eastern North America, *J. geophys. Res.*, **85**, 5212–5218.

Mitchell, B. J. & Hwang, H. J., 1987. Effect of low *Q* sediments and crustal *Q* on *Lg* attenuation in the United States, *Bull. seism. Soc. Am.*, **77**, 1197–1210.

Montagner, J. P., 1986. Regional three-dimensional structures using long-period surface waves, *Ann. Geophys.*, **4**, 283–294.

Moreau, C., Regnoult, J-M., Deruelle, B. & Robineau, 1987. A new tectonic model for the Cameroon line, central Africa, *Tectonophysics*, **139**, 317–334.

Morgan, P., 1982. Heat flow in rift zones, in *Continental and Oceanic Rifts, ed.* Palmason, G., *Geodynamics Series*, **8**, American Geophysical Union, Washington DC, Geological Society of America, Boulder, Colorado.

Nolet, G., 1987. Seismic wave propagation and seismic tomography, in *Seismic Tomography with Applications in Global Seismology and Exploration Geophysics*, ed. Nolet, G., Reidel, Dordrecht.

Nuttli, O. W., 1988. *Lg* magnitudes and yield estimates for underground Novaya Zemlya nuclear explosions, *Bull. seism. Soc. Am.*, **78**, 873–884.

O'Connell, R. J. & Budianski, B., 1977. Viscoelastic properties of fluid-saturated cracked solids, *J. geophys. Res.*, **82**, 5719–5735.

Raoof, M. & Nuttli, O. W., 1985. Attenuation of high-frequency earthquake waves in south America, *Pure appl. Geophys.*, **22**, 619–644.

Singh, S. K. & Herrmann, R. B., 1983. Regionalization of crustal coda *Q* in the continental United States, *J. geophys. Res.*, **88**, 527–538.

Snieder, R., 1987. Surface wave holography, in *Seismic Tomography with Applications in Global Seismology and Exploration Geophysics*, ed. Nolet, G., Reidel, Dordrecht.

Suetsugu, D. & Nakanishi, I., 1985. Tomographic inversion and resolution for Rayleigh wave phase velocities in the Pacific Ocean, *J. Phys. Earth*, **33**, 345–368.

Winkler, K. & Nur, A., 1979. Pore fluids and seismic attenuation in rocks, *Geophys. Res. Lett.*, **6**, 1–4.

Xie, J. & Mitchell, B. J., 1988. Tomographic imaging of large scale lateral variations in *Lg* coda *Q*, *EOS Trans. Am. Geophys. Un.*, **69**, 1309.

Xie, J. & Nuttli, O. W., 1988. Interpretation of high-frequency coda at large distances: stochastic modeling and method of inversion, *Geophys. J.*, **95**, 579–595.